

# 1 Quantification of the dust optical depth across spatiotemporal scales with the 2 MIDAS global dataset (2003-2017)

3  
4 Antonis Gkikas<sup>1</sup>, Emmanouil Proestakis<sup>1</sup>, Vassilis Amiridis<sup>1</sup>, Stelios Kazadzis<sup>2,3</sup>, Enza Di Tomaso<sup>4</sup>,  
5 Eleni Marinou<sup>1,5</sup>, Nikos Hatzianastassiou<sup>6</sup>, Jasper F. Kok<sup>7</sup> and Carlos Pérez García-Pando<sup>4,8</sup>

6  
7 <sup>1</sup>Institute for Astronomy, Astrophysics, Space Applications and Remote Sensing, National Observatory of Athens,  
8 Athens, 15236, Greece

9 <sup>2</sup>Physikalisch-Meteorologisches Observatorium Davos, World Radiation Center, Switzerland

10 <sup>3</sup>Institute of Environmental Research and Sustainable Development, National Observatory of Athens, Greece

11 <sup>4</sup>Barcelona Supercomputing Center, Barcelona, Spain

12 <sup>5</sup>Deutsches Zentrum für Luft- und Raumfahrt (DLR), Institut für Physik der Atmosphäre, Oberpfaffenhofen, Germany

13 <sup>6</sup>Laboratory of Meteorology, Department of Physics, University of Ioannina, Ioannina, Greece

14 <sup>7</sup>Department of Atmospheric and Oceanic Sciences, University of California, Los Angeles, CA 90095, USA

15 <sup>8</sup>ICREA, Catalan Institution for Research and Advanced Studies, Barcelona, Spain

16

17  
18 Corresponding author: Antonis Gkikas (agkikas@noa.gr)

19

## 20 Abstract

21 Quantifying the dust optical depth (DOD) and its uncertainty across spatiotemporal scales is key to  
22 understanding and constraining the dust cycle and its interactions with the Earth System. This study  
23 quantifies the DOD along with its monthly and year-to-year variability between 2003 and 2017 at  
24 global and regional levels based on the MIDAS (ModIs Dust AeroSol) dataset, which combines  
25 MODIS-Aqua retrievals and MERRA-2 reanalysis products. We also describe the annual and  
26 seasonal geographical distributions of DOD across the main dust source regions and transport  
27 pathways. MIDAS provides columnar mid-visible (550 nm) DOD at fine spatial resolution ( $0.1^\circ \times$   
28  $0.1^\circ$ ), expanding the current observational capabilities for monitoring the highly variable  
29 spatiotemporal features of the dust burden. We obtain a global DOD of  $0.032 \pm 0.003$  – approximately  
30 a quarter ( $23.4\% \pm 2.4\%$ ) of the global aerosol optical depth (AOD) – with about one order of  
31 magnitude more DOD in the northern hemisphere ( $0.056 \pm 0.004$ ;  $31.8\% \pm 2.7\%$ ) than in the southern  
32 hemisphere ( $0.008 \pm 0.001$ ;  $8.2\% \pm 1.1\%$ ) and about 3.5 times more DOD over land ( $0.070 \pm 0.005$ )  
33 than over ocean ( $0.019 \pm 0.002$ ). The northern hemisphere monthly DOD is highly correlated with  
34 the corresponding monthly AOD ( $R^2=0.94$ ) and contributes 20% to 48% of it, both indicating a  
35 dominant dust contribution. In contrast, the contribution of dust to the monthly AOD does not exceed  
36 17% in the southern hemisphere, although the uncertainty in this region is larger. Among the major  
37 dust sources of the planet, the maximum DODs ( $\sim 1.2$ ) are recorded in the Bodélé Depression of the

38 northern Lake Chad Basin, whereas moderate-to-high intensities are encountered in the Western  
39 Sahara (boreal summer), along the eastern parts of the Middle East (boreal summer) and in the  
40 Taklamakan Desert (spring). Over oceans, major long-range dust transport is observed primarily  
41 along the Tropical Atlantic (intensified during boreal summer) and secondarily in the North Pacific  
42 (intensified during boreal spring). Our calculated global and regional averages and associated  
43 uncertainties are consistent with some but not all recent observationally based studies. Our work  
44 provides a simple, yet flexible method to estimate consistent uncertainties across spatiotemporal  
45 scales, which will enhance the use of the MIDAS dataset in a variety of future studies.

46

## 47 **1. Introduction**

48 Mineral dust particles are emitted throughout the year across the arid and semi-arid regions of the  
49 planet, when winds exceed a threshold velocity mainly determined by soil texture, soil moisture, and  
50 surface roughness. While dust aerosols have mainly a natural origin, the contribution of  
51 anthropogenic land use is estimated to be between 10% and 25 % (Tegen et al. 2004; Stanelle et al.,  
52 2014; Ginoux et al., 2012). Dust is mobilized by microscale to synoptic scale phenomena, from dust  
53 devils developed under strong surface heating (Koch and Renno, 2005), to “haboobs” formed by  
54 intense cold-pool downdrafts related to deep moist convection (Knippertz et al., 2007), to synoptic  
55 patterns associated with intensified pressure gradients (Klose et al., 2010) and low-level jets (LLJ;  
56 Fiedler et al., 2013). Meteorology also plays a key role in the dust transport over maritime areas taking  
57 place mainly across the Tropical Atlantic Ocean (Prospero and Mayol-Bracero, 2013; Yu et al., 2015),  
58 the northern Pacific Ocean (Husar et al., 2001), the Mediterranean (Flaounas et al., 2015; Gkikas et  
59 al., 2015), the Arabian Sea (Ramaswamy et al., 2017) and the southern Atlantic Ocean (Gasso and  
60 Stein, 2007). Dust perturbs the radiation budget through direct (Sokolik and Toon, 1996), semi-direct  
61 (Huang et al., 2006) and indirect (Haywood and Bucher, 2000) processes, leading to impacts upon  
62 weather (Pérez et al., 2006; Gkikas et al., 2018; Gkikas et al., 2019) and climate (Lambert et al., 2013;  
63 Nabat et al., 2015). Upon deposition, nutrient-rich dust particles can increase the productivity of  
64 oceanic waters (Jickells et al., 2005) and terrestrial ecosystems (Okin et al., 2004) and perturb the  
65 carbon cycle (Jickells et al., 2014). Dust has been associated with epidemics of meningococcal  
66 meningitis in the African Sahel (Pérez García-Pando et al., 2014a, b) and with air quality degradation  
67 in urban areas (Kanakidou et al., 2011) causing respiratory (Kanatani et al., 2010) and cardiovascular  
68 (Du et al., 2016) disease when the population is exposed to high dust concentrations (Querol et al.,  
69 2019). Other socio-economic sectors can be regionally affected by dust storms (Middleton, 2017),  
70 including transportation (Weinzierl et al., 2012), agriculture (Stefanski and Sivakumar, 2009) and  
71 solar energy production (Kosmopoulos et al., 2018).

72 Satellite measurements and numerical simulations have repeatedly shown the remarkable contrast  
73 in dust load between the two hemispheres. The substantially higher dust load in the N. Hemisphere  
74 is associated to the wider deserts extending across the so-called “dust belt” (Prospero et al., 2002;  
75 Ginoux et al., 2012) in contrast to the smaller sources in Australia, South Africa and South America.  
76 At global scale, most of the entrained dust loads in the atmosphere originate from tropical and sub-  
77 tropical arid regions; yet, it is estimated that up to 5% of the global dust budget consists of particles  
78 emitted from high-latitude sources (Bullard and Austin, 2011; Bullard et al., 2016). Given the key  
79 role of dust aerosols in the Earth system it is imperative to monitor and understand the global dust  
80 cycle along with its multi-scale spatiotemporal variability over long time periods and fine spatial  
81 resolution. This task can be fulfilled to a certain degree using contemporary satellite instruments  
82 providing accurate retrievals and global coverage over extended time periods. With this approach,  
83 one of the key challenges is to discriminate dust from other aerosols. Several studies have combined  
84 AOD and aerosol index (AI) (e.g., Middleton and Goudie, 2001; Prospero et al., 2002) or AOD, single  
85 scattering albedo (SSA) and Ångström exponent (AE) (Ginoux et al., 2012) to identify the most active  
86 dust sources worldwide. Other studies have focused on the dust load and its variability in specific  
87 regions such as the Atlantic Ocean and the Arabian Sea (Peyridieu et al., 2013), the Sistan basin  
88 (Rashki et al., 2015), the Mediterranean (Gkikas et al., 2016), Europe and North Africa (Marinou et  
89 al., 2017) and east Asia (Proestakis et al., 2018), among others. Liu et al. (2008) described the three-  
90 dimensional structure of dust aerosols at global scale based on CALIOP vertically resolved retrievals  
91 acquired during the first operational year of the CALIPSO satellite mission. A more advanced  
92 approach has been introduced by Amiridis et al. (2013) and Marinou et al. (2017), who applied a  
93 more realistic lidar ratio for the Saharan dust and a series of quality filters on the CALIOP vertical  
94 profiles, in order to provide information about the vertical structure of dust layers at global scale and  
95 coarse resolution in the LIVAS dataset (Amiridis et al., 2015). Ridley et al. (2016) quantified the  
96 global average DOD and its uncertainty for the period 2004-2008 based on AOD retrievals from  
97 passive spaceborne sensors (MODIS, MISR), ground-based (AERONET) and shipborne (MAN)  
98 measurements from sun-photometers, and numerical simulations. Voss and Evan (2020) provided a  
99 long-term DOD climatology over the Tropics and mid-latitudes at a coarse spatial resolution ( $1^\circ \times$   
100  $1^\circ$ ) based on MODIS and AVHRR observations, where DOD was estimated based on AOD, SSA and  
101 AE over land following Ginoux et al. (2012) and AOD, fine and coarse AOD (AERONET) and  
102 MERRA-2 winds over ocean. Based on vertically-resolved CALIOP retrievals and columnar MODIS  
103 optical properties, Song et al. (2021) provided a long-term 4D global dust optical depth dataset,  
104 excluding the polar regions, over the period 2007 – 2019. In their approach, they took advantage of  
105 spaceborne observations that can be used for the discrimination/identification of dust aerosols  
106 characterized by their aspherical shape, coarse size and absorption.

107 Our study provides a global and regional quantification and description of the DOD based on the  
108 new ModIs Dust AeroSol (MIDAS) dataset (Gkikas et al., 2021). The powerful and innovative  
109 elements of the MIDAS DOD dataset are the: (i) daily availability and fine spatial resolution ( $0.1^\circ \times$   
110  $0.1^\circ$ ), (ii) full global coverage including the sources and downwind areas (both over land and sea),  
111 (iii) 15-year temporal range (2003 – 2017) using the most updated MODIS data collection, (iv) grid-  
112 cell level uncertainty quantification. In this contribution, we first describe the annual and seasonal  
113 geographical distribution of DOD across the main dust source regions and transport pathways  
114 (Section 4.1). We then quantify the average DOD and its monthly and year-to-year variability at  
115 global, hemispherical and regional levels, along with its fractional contribution to the AOD (Section  
116 4.2). We summarize the main findings in Section 5.

## 117 **2. ModIs Dust AeroSol (MIDAS) dataset**

118 Our study is based on the MIDAS global fine resolution dataset described in detail in Gkikas et  
119 al. (2021). We analyse the DOD at 550 nm, at  $0.1^\circ \times 0.1^\circ$  spatial resolution, between 2003 to 2017.  
120 The MIDAS DOD results from the combination of the quality-filtered MODIS aerosol optical depth  
121 (AOD, Collection 6.1, Level 2; Levy et al., 2013) and the MERRA-2 (Modern-Era Retrospective  
122 Analysis for Research and Applications, version 2; Gelaro et al., 2017) fraction of AOD that is due  
123 to dust (MDF). In Gkikas et al. (2021), the MDF was evaluated against the dust fraction obtained  
124 from quality-assured dust and non-dust CALIOP (Cloud-Aerosol Lidar with Orthogonal Polarization;  
125 Winker et al., 2009) profiles, available from the LIVAS database (Amiridis et al., 2015; Marinou et  
126 al., 2017; Proestakis et al., 2018). The MDF compares well with the LIVAS dust fraction over the  
127 dust-abundant areas extending across the NH dust belt, with maximum underestimations of 10 % in  
128 Asian deserts. The agreement is more limited in North America and the Southern Hemisphere  
129 (Figures 1 and 2 in Gkikas et al., 2021). Overall, the MIDAS DOD is well correlated with AERONET  
130 dust-dominant retrievals ( $R=0.89$  at global scale) and the absolute biases are mainly below 0.12 at  
131 stations near sources (Figures 3 and 4 in Gkikas et al., 2021). The MIDAS DOD dataset was further  
132 verified against the LIVAS DOD and compared with MERRA-2 DODs (Figure 5 in Gkikas et al.,  
133 2021). Among the three datasets, there is good agreement on the monthly variability of the global and  
134 hemispherical DODs as well as on their long-term averages (Figure 6 and Table 1 in Gkikas et al.,  
135 2021). Moreover, the annual and seasonal DOD patterns are broadly similar in the three datasets  
136 throughout the period 2007 – 2015. Nevertheless, regionally differences are found due to the different  
137 techniques (passive and active remote sensing, numerical simulations) applied for the DOD  
138 derivation.

139

140

### 141 3. Spatiotemporal averaging and propagation of grid-cell level uncertainties

142 In section 4.2 we provide DOD estimates that are averaged in space (regionally and globally) and  
143 in time (over months, seasons and years) along with their respective uncertainties. Averaging is  
144 performed according to the upper branch of Figure 5 in Levy et al. (2009), i.e. spatial averaging is  
145 performed after grid cell temporal averaging for any of the timescales considered. The uncertainties  
146 of the DOD averages at the different spatiotemporal scales are based on the propagation of the daily  
147 grid cell uncertainties provided within the MIDAS dataset and presented in Gkikas et al. (2021). In  
148 short, the daily grid cell uncertainties combine the uncertainties of the MODIS AOD and the  
149 MERRA-2 MDF with respect to AERONET and LIVAS, respectively. The former is based on linear  
150 equations expressing the uncertainty with respect to AERONET AOD over ocean (Levy et al., 2013)  
151 and land (Levy et al., 2010; Sayer et al. 2013) with updated coefficients for C061 data depending on  
152 vegetated and arid surface types (see equations 4 to 7 in Gkikas et al., 2021). The latter is based on a  
153 quartic (fourth degree) polynomial equation expressing the uncertainty with respect to the LIVAS  
154 dust fraction (see equation 8 in Gkikas et al., 2021).

155 In order to estimate the uncertainties of the spatiotemporal averages we first assume that each of  
156 the daily grid cell uncertainties are composed of (1) a fraction that is completely random in time and  
157 space, (2) a fraction that is systematic (correlated) in time and random in space and (3) a fraction that  
158 is systematic (correlated) in space and random in time. Our framework also assumes that the fraction  
159 of the daily grid cell uncertainty that is correlated both in space and time, for instance an instrument  
160 bias, is very small and therefore neglected. Under this framework, the propagation of uncertainty  
161 fraction (1) is negligible across the spatiotemporal scales considered, the propagation of uncertainty  
162 fraction (2) depends upon the size of the domain considered but is negligible at global scale and across  
163 most of the regional domains considered in this study, and propagation of fraction (3) accounts for  
164 most of the total average uncertainty. Since we cannot know fractions (1), (2) and (3) and (1) and (2)  
165 are negligible or small, we assume that (3) represents 100 % of the uncertainty, i.e the grid cell  
166 uncertainty is systematic (correlated) in space and random in time, to provide an upper limit on the  
167 uncertainty. In addition, we also take into account the sampling uncertainty when temporally  
168 averaging over each grid cell using the standard error, i.e., we take the standard deviation divided by  
169 the square root of the number of measurements.

170 In practice, when averaging the daily values for every grid cell  $i$  over months, seasons, or years,  
171 the uncertainty  $\sigma'_i$  is obtained by adding in quadrature the daily uncertainties  $\sigma_{N_i}^2$  and dividing by the  
172 number of available daily measurements  $N_i$ :

$$173 \sigma'_i = \frac{\sqrt{\sigma_{i,1}^2 + \sigma_{i,2}^2 + \dots + \sigma_{N_i}^2}}{N_i} \text{ (Eq. 1)}$$

174

175 In addition, we add in quadrature  $\sigma'_i$  and the standard error  $SE_i$  to obtain the total uncertainty of  
176 the temporal average  $\sigma_i$  for every grid cell:

177

$$178 \quad \sigma_i = \sqrt{\sigma'^2_i + SE^2_i} \text{ (Eq. 2)}$$

$$179 \quad SE_i = \frac{SD_i}{\sqrt{N_i}} \text{ (Eq. 3)}$$

180

181 where  $SD_i$  is the standard deviation of the daily values in grid cell  $i$ . The standard error measures how  
182 far the sample could be from the true population mean.

183 Finally, when spatially averaging globally or regionally, under the assumption that the errors are  
184 correlated across space, the overall uncertainty is calculated by averaging  $\sigma_i$  across the  $N_j$  grid cells  
185 in spatial domain  $j$  weighted by the grid cell area fraction with respect to the total area (i.e., grid cell  
186 / total area =  $w_i$ ) with available retrievals:

187

$$188 \quad \sigma_j = \sum_{i=1}^{N_j} w_i * \sigma_i \text{ (Eq.4)}$$

189

## 190 **4. Results**

191

192 Our analysis is divided in two main parts. In the first one (Section 4.1) we assess the annual and  
193 seasonal climatological DOD maps for nine distinct regions. In the second one (Section 4.2),  
194 emphasis is given on the quantification of DOD averages along with their monthly and interannual  
195 variability of the fractional contribution to the AOD, from a global to hemispherical level as well as  
196 for specific regional domains.

197

### 198 *4.1 Annual and seasonal geographical distributions of DOD*

199

#### 200 *4.1.1 North Africa, Tropical Atlantic Ocean and Mediterranean*

201

202 According to the long-term average map (Fig. 1), the maximum DODs (up to 1.2) are recorded in  
203 the Bodélé depression, which is considered the most active individual dust source of the planet  
204 (Washington et al., 2003; Koren et al., 2006; Ginoux et al., 2012). Over the area, the prevailing strong  
205 winds are intensified further between the Tibesti mountains and the Ennedi ridge (Washington et al.,  
206 2009) forming a low-level jet (Washington and Todd, 2005). This dominant wind pattern, affected  
207 by the local topography (Washington et al., 2009), acts as the driving force mobilizing mineral  
208 particles from arid and erodible soils of the region (Tegen et al., 2006). Under these favorable

209 conditions, dust aerosols are easily uplifted and accumulated in the atmosphere thus causing the very  
210 high DODs ( $> 0.5$ ) observed in the broader area (Chad, Niger). Throughout the year, the high DOD  
211 levels are quite persistent exhibiting, however, a seasonal variation with more intense loads recorded  
212 during DJF (Fig. S1-i) and MAM (Fig. S1-ii) following the annual cycle of source activation  
213 (Washington et al., 2009). The second hotspot in N. Africa is situated between the northern parts of  
214 Nigeria and the southern parts of Niger with annual DODs reaching up to 0.7 (Fig. 1) while on  
215 seasonal basis vary from 0.4 (SON; Fig. S1-iv) to 0.8 (JJA; Fig. S1-iii). MIDAS DODs match well  
216 with those presented by Rajot et al. (2008), who relied on ground-based sunphotometric  
217 measurements of AOD obtained at the Banizoumbou AERONET site. Very high DODs are also  
218 evident along the coasts of the Gulf of Guinea, which may be unrealistic considering that dust aerosols  
219 are mainly transported there and are mixed with anthropogenic and biomass burning (Knippertz et  
220 al., 2015). Along this area of high DODs, MERRA-2 also overestimates the dust fraction compared  
221 to LIVAS (Gkikas et al., 2021) thus resulting in higher intensities according to the applied  
222 methodology (Section 2). Moreover, the temporal availability of DODs in the region is very limited  
223 ( $<10\%$ ; Fig. 8-c in Gkikas et al., 2021), the DOD uncertainty is large and AOD outliers, either realistic  
224 or cloud contaminated, can yield exceptional high DODs in this complex environment where aerosol  
225 and clouds are spatially correlated (Andrew Sayer, personal communication). This abrupt reduction  
226 of DOD levels, from inland to the nearby maritime environment, reveals an artifact of the MIDAS  
227 dataset mainly introduced by the raw MODIS AOD retrievals, which are obtained by retrieval  
228 algorithms built on different assumptions/considerations depending on the underlying surface type.

229 Across the Sahara Desert, there is a distinct longitudinal contrast with more intense dust loads in  
230 western North Africa than in eastern North Africa (Fig. 1). In the former sector, the DODs range  
231 mainly from 0.3 to 0.6 while over the eastern parts of the Sahara the corresponding limits are bounded  
232 between 0.1 and 0.3 without revealing significant intra-annual variation. During MAM (Fig. S1-ii),  
233 along the southern Sahel, the activation of dust sources results in DODs which locally can exceed  
234 0.8, while during boreal summer (Fig. S1-iii) a vast area of the western Sahara is under the impact of  
235 heavy dust loadings ( $\text{DOD} > 0.5$ ). According to Ginoux et al. (2012), in the former region, dust is  
236 mainly produced by agricultural activities (cultivation, overgrazing) disturbing soils in which alluvial  
237 sediments have been accumulated. Northwards, dust has natural origin and the accumulation of  
238 mineral particles is favored by the development of the Saharan Heat Low (SHL) affecting also the  
239 prevailing airflow (harmattan winds) as well as the West African Monsoon (WAM) (Schepanski et  
240 al., 2017). Under these meteorological conditions, several dynamic processes, from microscale to  
241 mesoscale, are taking place triggering dust emission (Knippertz and Todd, 2012) from highly active  
242 sources (Schepanski et al., 2007).

243 Under the impact of the trade winds, Saharan dust can travel across the tropical Atlantic Ocean  
244 reaching the Caribbean Sea, the southern United States and northeastern South America (Prospero,  
245 1999; Prospero et al., 2014). The signal of this long-range transport is evident on the annual  
246 climatological pattern (Fig. 1) with DODs up to 0.6 (off the western Saharan coasts) fading down to  
247 0.1 at the maximum distance. Within the course of the year, the Saharan dust plume varies in terms  
248 of intensity, range and latitudinal position, as it is depicted in Figure S1. During boreal summer (Fig.  
249 S1-iii), the corridor of the transatlantic dust transport is bounded between 10° N and 20° N latitudes  
250 whereas both the intensity (DODs up to 0.6) and the range are maximized. During boreal winter (Fig.  
251 S1-i), the dust zone migrates southwards (between Equator and 10° N) while maximum (up to 0.6)  
252 and considerable (0.1-0.2) DODs are observed over the Gulf of Guinea and mid-Atlantic (45° W),  
253 respectively. Between the transition seasons (Fig. S1-ii, S1-iv), dust loads are stronger in MAM  
254 (~0.45), mainly residing within 5° N and 20° N latitudes, in contrast to SON (~0.3) when are shifted  
255 northwards (10° N and 25° N). According to the existing literature, several factors modulate the  
256 westwards propagation of dust plumes, originating in the western Sahara and the Bodélé Depression,  
257 over the tropical Atlantic. For instance, the south-north displacement of the Saharan plumes is driven  
258 by the location of the Intertropical Convergence Zone (ITCZ) and the disturbances of the African  
259 easterly jet (Knippertz and Todd, 2012; Doherty et al., 2012). Teleconnection patterns, such as the El  
260 Niño–Southern Oscillation (ENSO; Prospero and Lamb, 2003), the North Atlantic Oscillation (NAO;  
261 Ginoux et al., 2004) and the North African Dipole Index (NAFDI; Rodríguez et al., 2015) have been  
262 also studied in order to interpret the decadal variations of dust concentrations over the Atlantic.  
263 Likewise, the vegetation coverage across the Sahel as well as the wind speeds, determined by the  
264 prevailing atmospheric circulation, over the Sahara play a key role on the amount of the emitted dust  
265 particles.

266 Due to the vicinity of the largest deserts of the planet, the Mediterranean is affected by dust  
267 outbreaks throughout the year (Gkikas et al., 2013; 2016; Marinou et al., 2017). Mineral particles  
268 originating primarily from north African and secondarily from Middle Eastern deserts are transported  
269 towards the Mediterranean mainly under the prevalence of cyclonic systems (Gkikas et al., 2015).  
270 The intensity of dust loads decreases for increasing latitudes, forming a distinct south-north gradient  
271 with DODs up to 0.20 between the gulfs of Gabes (Tunisia) and Sidra (Libya), according to the annual  
272 pattern (Fig. 1). Among seasons (Fig. S1), DODs vary on the locations where the maximum levels  
273 are recorded as well as on their magnitude, attributed to the position of the prevailing synoptic systems  
274 (Gkikas et al., 2015). The central and eastern Mediterranean sectors are affected by dust loads mainly  
275 in spring (DODs up to 0.3; Fig. S1-ii) and winter (DODs up to 0.12; Fig. S1-i). In summer (Fig. S1-  
276 iii), dust activity is more pronounced in the western parts with optical depths up to 0.18 (Alboran  
277 Sea), while thanks to the fine resolution product, “hotspots” of similar DODs can be identified in the



278 southern parts (Andalucia) of Spain. In SON (Fig. S1-iv), dust loads are found in the central  
279 Mediterranean with DODs lower than 0.12 off the Tunisian and Libyan coasts.

280

#### 281 4.1.2 *Middle East*

282

283 In the Middle East, there is a zone of moderate-to-high DODs (locally up to 0.8) extending from  
284 Mesopotamia to the southern parts of the Saudi Arabia, where one of the largest sand deserts of the  
285 world (Rub' al Khali) (Hamidi et al., 2013) is situated (Fig. 2). Based on Ginoux et al. (2012), the  
286 origin of mineral particles between Tigris and Euphrates as well as across the Rub' al Khali Desert is  
287 mainly natural while in the intermediate part (Ad-Dahna Desert) dust accumulation is attributed to  
288 the mixing of anthropogenic and hydrological sources. Slightly higher maximum DODs (up to 0.7;  
289 Fig. 2) are recorded in Oman and particularly between Dhofar and Al Wusta, in contrast to previous  
290 studies (Pease et al., 1998) which have identified the Wahiba Sands area as a major dust source or the  
291 coastal areas of Yemen (Ginoux et al., 2012). On a seasonal basis, the intensity of mineral loads  
292 exhibits a strong variability with minimum DODs (up to 0.4) during DJF (Fig. S2-i) and SON (Fig.  
293 S2-iv) and maximum (up to 1) during the dry period of the year (Figs S2-ii, S2-iii), being in agreement  
294 with the results presented in Yu et al. (2013). More specifically, across the Arabian Peninsula, the  
295 increase in DOD levels is getting evident in boreal spring and it is further intensified during summer  
296 months. Dust storms emanating in Iraq and the eastern parts of Saudi Arabia favor dust transport  
297 towards the Persian Gulf (Gianakopoulou and Toumi, 2012) account for the considerable high DOD  
298 levels ( $>0.6$ ) found there. Due to convergence of the northern-northernwesterly Shamal winds (Yu et  
299 al., 2016) and the airflow from the subtropical anticyclone, in JJA, mineral particles are travelling at  
300 even longer distances towards the northern Arabian Sea (Ramaswamy et al., 2017), as indicated by  
301 the intense dust loads (DODs up to 0.5; Fig. S2-iii) contributing about half of the AOD (Jin et al.,  
302 2018). Likewise, during boreal summer, short-range dust transport takes place off the coasts of Oman  
303 and Yemen (Gulf of Aden). Among seas in the vicinity of the Arabian Peninsula, the most intense  
304 dust loads are observed in the Red Sea, forming a clear latitudinal gradient on annual (Fig. 2) and  
305 summer (Fig. S2-iii) geographical DOD patterns, as it has been noted also in Brindley et al. (2015)  
306 and Banks et al. (2017). Due to its location, the southern sector of the Red Sea receives dust aerosols  
307 either originating from the Republic of Sudan or from the Arabian Peninsula, depending on the zonal  
308 airflow (Banks et al., 2017). Dusty air masses travelling westwards are uplifted when they are  
309 crossing the mountain range in the southwestern Arabian Peninsula and for this reason dust loads  
310 over the southern basin are suspended above 2 km (Banks et al., 2017). On the contrary, low-elevated  
311 dust layers are recorded when winds blow from west, triggering dust emission from the Tokar Gap  
312 (Sudanese coasts) and subsequently dust outflows into the southern Red Sea (Banks et al., 2017).

313

314 *4.1.3 Central and southwest Asia*

315

316 Northwards and eastwards of the Caspian Sea, various deserts are situated in the central segments  
317 of the Asian continent. Most part of Turkmenistan is occupied by the Karakum Desert while the  
318 Kyzylkum Desert is located in Uzbekistan. Other arid regions stretch between the Caspian and Aral  
319 Seas (Ustyurt plateau), in the eastern and southern flanks of the Aral Sea (Solonok Desert) and in the  
320 lowlands of western Kazakhstan and southeastern Russia (Ryn Desert) (Elguindi et al., 2016). Based  
321 on our seasonal spatial patterns (Fig. S3), the major dust activity is recorded in the Ustyurt Plateau  
322 (Li and Sokolik, 2018) and in the large lagoon embayment of Garabogazkol (Shen et al., 2016), a gulf  
323 of Turkmenistan dried into a salt-covered playa (Gills, 1996), with minimum (in DJF and SON) and  
324 maximum (in MAM and JJA) DODs equal to ~0.2 and ~0.4, respectively. In the rest of areas, the  
325 corresponding upper limits can reach up to 0.8-0.9, during boreal summer, in localized spots  
326 (Chimboy Lake, Sarygamysch Lake) across the Karakum and Kyzylkum Deserts. In the same season,  
327 moderate dust loadings (DOD up to 0.25) are encountered in the southern Caspian Sea (Elguindi et  
328 al., 2016) as the result of transported mineral particles mainly coming from the sandy deserts of  
329 Turkmenistan (Xi and Sokolik, 2015), under the impact of eastern/southeastern winds (Shen et al.,  
330 2016). Since the 1960s, the anthropogenic intervention (agricultural activities, over-irrigation) caused  
331 the retreat of the Aral Sea and the formation of the Aralkum Desert (Saiko and Zonn, 2000; Micklin,  
332 2007) from which large amounts of aeolian dust are emitted and travel distances of hundreds of  
333 kilometers (Indoitu et al., 2015). According to the annual climatological map (Fig. 3), extremely high  
334 DODs ( $> 1$ ) are found in the southeastern parts of the Aralkum Desert (Fig. 3) which are also  
335 persistent among the seasons (Fig. S3). Nevertheless, these are not trustworthy as it has been  
336 thoroughly discussed in Gkikas et al. (2021) (see Section 4.3.1).

337 In the Sistan basin, extending between Iran-Pakistan-Afghanistan, the long-term average JJA  
338 DODs can reach up to 1.1 (Figure S3-iii) in the Margo Desert (Afghanistan), due to the frequent  
339 occurrence of dust storms (Middleton, 1996), triggered by the northerly Levar winds, blowing from  
340 June to September (Alizadeh Choobari et al., 2014). These maximum DOD levels are substantially  
341 higher than the annual mean (0.8; Figure 3) as well as against the corresponding averages for the  
342 other seasons. Thanks to the high-resolution MIDAS DOD, we identify the borders of other active  
343 arid regions, surrounded by mountain ranges, such as the Rigestan (Afghanistan), the Balochistan  
344 (Pakistan), the Dasht-e-Kavir (Iran), the Dasht-e-Lut (Iran) and the Jazmurian drainage basin (Iran).  
345 In the aforementioned topographic lows, the magnitude of the dust loads is significantly lower than  
346 those observed in the Margo Desert and can be as large as 0.6 (Balochistan) during hot-dry months  
347 (Figure S3-iii). The presence of absorbing mineral particles, over the area and in the northernmost

348 part of the Arabian Sea, is also confirmed by the high AI values, especially in June-July, discussed  
349 by Rashki et al. (2015), who relied on long-term records obtained by the OMI and TOMS spaceborne  
350 sensors.

351

#### 352 *4.1.4 Indian subcontinent*

353

354 In the Indian subcontinent, the maximum annual DODs ( $\sim 0.5$ ; Fig. 4) are observed along the Indus  
355 river basin, in the western side of the Thar Desert whereas a branch of gradually decreasing DODs,  
356 along the Indo-Gangetic plain towards eastwards directions, is also evident. Ginoux et al. (2012)  
357 stated that much of dust activity in the Indus river basin is attributed to the suspension of soil particles  
358 originating primarily from agricultural land use and to a lesser extent from the desiccation of  
359 ephemeral water bodies. The strong presence of absorbing coarse particles over the area is further  
360 supported by the coexistence of considerably high Aerosol Index (AI) values (Alam et al., 2011). As  
361 indicated by the seasonal patterns (Fig. S4), the processes regulating the suspended dust loads are  
362 highly variable during the year causing a remarkable temporal variability of DOD, which is low ( $< 0.3$ )  
363 in DJF and SON, moderate in MAM ( $< 0.5$ ) and maximum in JJA ( $< 0.8$ ). Similar seasonal variability  
364 is evident in the Thar Desert, in agreement with the findings of Proestakis et al. (2018) and Dey and  
365 Di Girolamo (2010), who used vertically-resolved (CALIOP) and multi-angle (MISR) satellite  
366 retrievals, respectively. Nevertheless, our climatological DODs are higher with respect to the  
367 CALIOP corresponding values and the MISR non-spherical AODs, particularly when dust activity  
368 over the area is pronounced. During the pre-monsoon season, westerly to northwesterly winds are  
369 blowing over the Thar Desert mobilizing dust particles which subsequently are advected towards the  
370 Indo-Gangetic basin (Dey et al., 2004; Srivastava et al., 2011). According to our results, between the  
371 Haryana state and the eastern parts of the plain, DODs fade down from  $\sim 0.6$ - $0.7$  to  $\sim 0.1$ - $0.2$ , forming  
372 a NW-SE gradient (Figs. S4-ii, S4-iii). Such high DODs are attributed to the eastwards propagation  
373 of intense dust storms having a strong signature on the optical, microphysical and radiative properties  
374 derived by AERONET stations operating in the region (Prasad et al., 2007a; Prasad et al., 2007b; Eck  
375 et al., 2010).

376

#### 377 *4.1.5 East Asia and North Pacific Ocean*

378

379 Northwards of the Tibetan Plateau is located the Tarim Basin (northwest China) in which one of  
380 the largest natural dust source resides, the Taklamakan Desert. This elevated desert area (average  
381 elevation 1.1 km) is surrounded by the Pamir Plateau (average elevation 5.5 km) in its west side, by  
382 the Kunlun Shan range (average elevation 5.5 km) in its southern flanks and by the Tian Shan range

383 (average elevation 4.8 km) along its northern boundaries while only in its eastern margin the ground  
384 elevation is low (Ge et al., 2014). DODs are maximized in spring (Fig. S5-ii) yielding values up to 1  
385 along the foothills of the Tian Shan and Kunlun Shan ranges, attributed to the role of the topography  
386 on winds strengthening (Ge et al., 2014). Similar values are recorded in JJA (Fig. S5-iii) but the  
387 geographical distribution reveals that the highest DODs are less widespread in contrast to spring.  
388 Throughout the year, the weaker dust loads are recorded during winter and autumn. Our results are  
389 consistent with relevant studies that rely on active and passive satellite retrievals either of pure dust  
390 load (Proestakis et al., 2018) or AOD (de Leeuw et al., 2018; Sogacheva et al., 2018).

391 A common feature in the seasonal DOD patterns is the reduction of dust loads' intensity towards  
392 the interior parts of the Taklamakan Desert, as it has been also documented by Ge et al. (2014), who  
393 utilized MISR retrievals. The high-resolution of the MIDAS DOD dataset provides in detail the  
394 spatial information of these geographical patterns. During spring, similar high DODs to those found  
395 over the Taklamakan Desert are recorded in the Qaidam Basin (northeast side of the Tibetan Plateau),  
396 surrounded by the Atlun, Kunlun, Qilian mountain ranges, attributed to strong downslope winds  
397 causing the erosion of soil particles (Rohrmann et al., 2013) and their entrainment into the  
398 atmosphere. The intensity of dust loads over the Gobi Desert (north China – south Mongolia) hardly  
399 exceeds 0.3 on an annual basis (Fig. 5) while it can reach up to 0.4 during spring (Fig. S5-iii). The  
400 remarkable deviations in dust abundance between Taklamakan and Gobi during springtime are  
401 interpreted by variations in soil characteristics. More specifically, Taklamakan is composed mainly  
402 by fine sand particles in contrast to the rocky soils of the Gobi Desert (Sun et al., 2013). Due to these  
403 differences in soil textures, dust particles from the former desert region can be emitted even with low  
404 wind speeds while they are uplifted at higher elevations in the troposphere, as it has been shown with  
405 MISR stereo observations (Yu et al., 2019) and CALIOP lidar profiles (Proestakis et al., 2018). The  
406 injection of Taklamakan dust particles at higher altitudes increase their residence time inducing also  
407 their entrainment into the upper-level westerly airflow, around at 4 a.m.s.l., both contributing to the  
408 higher potential for long-range transport (Yu et al., 2019), in contrast to Gobi dust, towards the  
409 continental E. Asia and the northern Pacific Ocean. Under the impact of cold fronts, propagating  
410 eastwards (Eguchi et al., 2009) in spring, air masses carrying mineral particles, during the first two  
411 days of dust transport, affect a wide area of China (Yu et al., 2019), from near sources to its eastern  
412 parts, through the Hexi Corridor and the Loess Plateau (DODs ranging from 0.2 to 0.4; Fig. S5-iii).  
413 Subsequently, the Asian dust plumes are suspended over the Yellow Sea, the Korean Peninsula and  
414 further eastwards, in a latitudinal band bounded between the parallels 30°N and 45°, reaching the  
415 west coasts of the United States (Yu et al., 2008). Across this “belt”, where the Trans-pacific dust  
416 transport is taking place, the springtime DODs decrease smoothly from 0.15 to 0.05 (Fig. S5-ii). In  
417 summer (Fig. S5-iii), DODs up to 0.05 are observed between 40° N and 60° N indicating a northwards

418 displacement of the Asian dust layers (mainly originating from the Gobi Desert) due to the weakening  
419 and northwards shift of the polar jet streams (Yu et al., 2019).

420

#### 421 *4.1.6 North America*

422

423 Across N. America, the major dust activity is detected in southwest United States and in northwest  
424 Mexico with annual and seasonal DODs hardly exceeding 0.15, as illustrated in Figures 6 and S6,  
425 respectively. These weak dust load intensities are mainly recorded in the Sonoran and the Mojave  
426 Deserts while lower values are found in the Chihuahuan Desert in which isolated spots (e.g. White  
427 Sands Desert) become visible thanks to the high-resolution of the MIDAS DOD dataset. Low-to-  
428 moderate DODs are evident in the Great Plains with local maxima (exceeding 0.2 in spring; Fig. S6-  
429 ii) in the Great Salt Lake Desert and in the surrounding area as well as in the Baja Californian Desert  
430 (Mexico; DODs up to 0.14), residing in the western side of the Gulf of California. Our annual spatial  
431 distribution of DOD (Fig. 6) is highly consistent with those of frequency of observation (FoO) of  
432 DOD (Ginoux et al., 2012; Baddock et al., 2016) and AI given by Prospero et al. (2002). Moreover,  
433 the increase of dust loads' concentration in MAM (Fig. S6-ii), has been also documented by Hand et  
434 al. (2016) and Tong et al. (2017), both relying on aerosol observations acquired at numerous stations  
435 of the Interagency Monitoring of Protected Visual Environments (IMPROVE) network. During  
436 springtime, dust emission over the broader area is associated with the transmit of Pacific cold fronts  
437 inducing dust-entraining winds as the result of pressure gradient enhancement (Rivera Rivera et al.,  
438 2009). The geomorphological soil characteristics are determinant for dust emission with the most  
439 prominent natural sources being ephemeral and dry lakes (Baddock et al., 2016) while anthropogenic  
440 dust aerosols are mainly emitted in the Great Plains and in the eastern side of the Gulf of California  
441 (Ginoux et al., 2012).

442

#### 443 *4.1.7 Australia*

444

445 Earlier studies based on unconstrained numerical simulations (Tanaka and Chiba, 2006; Wagener  
446 et al., 2008) have shown that among the desert areas of the S. Hemisphere, the largest contribution of  
447 dust particles arises from Australia. However, a more recent assessment (Kok et al., 2021b) in which  
448 dust models have been constrained by observations revealed that the emitted dust amounts from S.  
449 America are slightly higher than those of Australia. Due to the fairly bright landmasses and the  
450 predominance of weak aerosol loadings, there is minimal contrast between surface and atmosphere  
451 leading to systematic algorithm uncertainties, which can explain the slightly lower land DODs than  
452 those recorded in the surrounding oceanic regions (Fig. 7 and S7). Nevertheless, in the sources as

453 well as in areas affected by dust plumes the atmospheric signal becomes evident. In particular, the  
454 highest dust emissions are encountered in the Lake Eyre Basin (LEB; Prospero et al., 2002) composed  
455 by ephemeral lakes, alluvial channels, gibber (stone-covered plains), aeolian sand deposits and  
456 bedrocks (Bullard et al., 2008). Based on the annual climatological pattern (Fig. 7), DODs can locally  
457 exceed 0.2 (in the southern parts) but in general vary between 0.06 and 0.12. From a seasonal  
458 perspective (Fig. S7), the highest DODs (mainly up to 0.18 in the Warburton River estuary, few  
459 exceedances above 0.4 are found in local spots) are recorded during austral summer (DJF; Fig. S7-i)  
460 and spring (SON; Fig. S7-iv). Similar seasonal variation in ground-based sunphotometric  
461 observations at nearby sites (Birdsville, Tinga Tingana), with slightly lower AODs, has been reported  
462 by Mitchell et al. (2017). Southwards of the LEB, three spots of notable DODs (up to 0.2 in SON;  
463 Fig. S7-iv) are identified in the Lakes Gairdner, Torrens and Frome while northeastwards (Lake  
464 Yamma Yamma) and northwards (Simpson Desert) from the basin the suspended dust loads exhibit  
465 optical depths as large as 0.12 during the driest months of the year. Similar maximum DODs are  
466 recorded in the Northern Territory and in the western side of the Great Dividing Range (Queensland)  
467 and in contrast to Ginoux et al. (2012) these levels appear in DJF instead of SON. In the southwestern  
468 coastal parts of the Australian landmass as well as in Riverina (southeast), during austral spring (Fig.  
469 S7-iv) very low DODs are evident associated with anthropogenic dust originating from agricultural  
470 activities (Ginoux et al., 2012). Finally, during the same season, weak signals (DODs up to 0.05) of  
471 dust transport are revealed over the Tasman and Timor Seas attributed to the eastward movement of  
472 cyclonic frontal systems causing the entrainment of mineral particles in air masses that can travel at  
473 long distances (Knight et al., 1995; Choobari et al., 2012).

474

#### 475 *4.1.8 South Africa*

476

477 Dust activity in S. Africa is mainly related with short-range and short-lived plumes (Vickery et  
478 al., 2013) that are suspended at low tropospheric altitudes (below 600 hPa) due to the predominance  
479 of anticyclonic circulations inhibiting the vertical extension of dust layers (Piketh et al., 1999).  
480 Mineral aerosol loadings are mainly originating from the ephemeral lake basins of the Etosha Pans  
481 (Namibia) and Makgadikgadi Pans (Botswana) and the Namib Desert (Bryant et al., 2007; Vickery  
482 et al., 2013). In the aforementioned source areas, the maximum annual (Figure 8) and seasonal (Figure  
483 S8) DODs are equal to 0.1 and 0.16, respectively. Throughout the year, the increase of DODs in  
484 Etosha and Makgadikgadi Pans is evident primarily in DJF (Figure S8-i) and secondarily in SON  
485 (Figure S8-iv). Our results are consistent with those provided by Ginoux et al. (2012) and Bryant et  
486 al. (2007) for the former region (including also the Kalahari Desert in which very weak dust loads are  
487 recorded), contradictory for the latter one and opposite with the findings of Vickery et al. (2013) for

488 both sources. In these arid areas dust emission is linked with lakes' inundation, characterized by  
489 strong intra-annual variability, playing an important role when different time periods are considered.  
490 However, it must be also taken into account the moderate performance of the MERRA-2 dust portion  
491 with respect to LIVAS in S. Africa as well as in most desert areas of the S. Hemisphere (Gkikas et  
492 al., 2021). Along the Namibian coastline, the deviations of DOD between the high- and low-dust  
493 seasons are small indicating that dust activity remains relatively constant within the course of the year  
494 (Ginoux et al., 2012). Soil particles from salt pans and dry river beds of the Namib Desert are emitted  
495 from aeolian processes related to bergwinds (katabatic winds) blowing in the escarpment, from the  
496 Central Plateau down to the coasts (Eckardt and Kuring, 2005). Dust outflow towards the Southern  
497 Atlantic Ocean, with a SE-NW orientation, it is shown between 18° S and 9° S during austral winter  
498 (DODs up to 0.08; Fig. S8-iii), becoming more evident in SON (Fig. S8-iv), being in agreement with  
499 the geographical distributions provided by Voss and Evan (2020). Such transport is favored by the  
500 propagation of barotropic low-level easterly waves formed between continental high pressure systems  
501 and the semi-permanent South Atlantic anticyclone (Tyson et al., 1996). Finally, weak signals of  
502 DODs are recorded in the croplands north of Cape Town, with annual and DJF DODs not exceeding  
503 0.1.

504

#### 505 *4.1.9 South America*

506

507 In South America, the most intense dust loads are encountered in the Patagonia Desert where the  
508 most active dust sources are situated in the river basins of the Rio Negro and Chubut provinces and  
509 in its southern end. Among these areas, higher DODs (up to 0.16 in DJF; Figure S9-i) are found along  
510 the Rio Negro attributed to anthropogenic dust originating from overgrazing, irrigation and oil  
511 prospecting (McConnell, et al., 2007; Mazzonia and Vazquez, 2009). In southern latitudes, mineral  
512 particles originate from glacier washout plains (Hernández et al., 2008). Under favorable  
513 meteorological conditions, aeolian dust from Patagonia travels either towards the southern Atlantic  
514 Ocean, contributing to iron concentrations and marine biological productivity in the surface waters  
515 (Johnson et al., 2011), or towards the Antarctica peninsula (Gassó et al., 2010), as it has been found  
516 in ice core samples (Basile et al., 1997). Both transport pathways are not visible in our climatological  
517 patterns (Figures 9 and S9) since dust outbreaks are not so strong (Foth et al., 2019) while the  
518 extended cloud coverage over the region results in large observational gaps of the spaceborne  
519 retrievals (Gassó and Torres, 2019). Along the western side of Andes, dust emission arises from  
520 natural sources located in the Sechura (Peru), Nazca (Peru) and Atacama (Chile) Deserts (Ginoux et  
521 al., 2012). In the aforementioned regions, the annual DODs (Figure 9) can reach up to 0.1, 0.08 and  
522 0.06, respectively, while the intra-annual variability is characterized weak (Figure S9). During MAM

523 (Figure S9-ii), DODs up to 0.16 appear in Guyana, Suriname and French Guiana as well as over their  
524 offshore areas while similar intensities are evident in the northern parts of the Amazon rainforest  
525 (around the Equator and bounded between 65°W and 60°W). The presence of coarse mineral particles  
526 (Moran-Zuloaga, et al., 2018) over these distant areas from deserts, is attributed to the long-range  
527 dust transport from North Africa across the Atlantic Ocean (Yu et al., 2015), under the impact of the  
528 trade winds, taking place northwards of the convective precipitation zone formed around the ITCZ.  
529 Finally, the latitudinal zone of weak DODs in the western parts of Brazil, fading down abruptly  
530 eastwards of ~58° W, indicates an artifact of the MIDAS product that becomes more evident in SON  
531 (Fig. S9-iv). This peculiar pattern is induced by the MERRA-2 dust fraction (results not shown here)  
532 which is used for the derivation of MIDAS DOD from the MODIS AOD. An additional deficiency is  
533 the relatively large DODs over an area where biomass burning particles, emitted at enormous amounts  
534 by extended wildfires, clearly dominate over other aerosol species. Under these conditions, the non-  
535 dust AODs are very high as well as their relevant uncertainties (Eqs. 5-7 in Gkikas et al. (2021)) while  
536 the reliability of the MERRA-2 dust fraction downgrades there (see Fig. 2 in Gkikas et al. (2021)).

537

#### 538 *4.2 DOD averages and variability at global, hemispherical and regional scales*

539

540 In this section, we discuss the average AOD and DOD along with their monthly and interannual  
541 variability at global, hemispherical and regional scales. The left column of Figure 10 shows the  
542 interannual timeseries of AOD (black curve) and DOD (red curve) averaged over the whole globe  
543 (upper panel; GLB), the Northern Hemisphere (middle panel; NHE) and the Southern Hemisphere  
544 (bottom panel; SHE). The right column of Figure 10 depicts the monthly seasonal cycle of AOD and  
545 DOD along with the DOD-to-AOD ratio (blue curve) while the shaded areas correspond to the total  
546 uncertainty (see Section 3.2 in Gkikas et al. (2021) and Section 3 in the current study).

547 The significant role of dust particles in the global aerosol budget becomes evident by visually  
548 inspecting the AOD and DOD interannual timeseries (Fig. 10 i-a). The monthly contribution of  
549 suspended dust to the total AOD varies from 14% to 39%, with minimum values mainly in DJF and  
550 maximum values in MAM or JJA, depending on the year. Monthly DODs range from  $0.016 \pm 0.013$   
551 (Dec 2005) to  $0.063 \pm 0.028$  (Mar 2012), whereas the long-term global annual average is equal to  
552  $0.032 \pm 0.003$  (Table 1). The global DOD mean, computed here from the fine resolution data, is  
553 almost identical with those obtained by the coarse spatial resolution MERRA-2 and MIDAS DODs  
554 and slightly higher than those calculated based on LIVAS-CALIOP (0.029) (see Table 1 in Gkikas et  
555 al. (2021); it is noted the three datasets had been collocated based on the spatial resolution and the  
556 temporal availability of the LIVAS dataset). Likewise, our global average and uncertainty computed  
557 over the period 2004-2008 ( $0.033 \pm 0.004$ ) is close to the one obtained in Ridley et al. (2016) (0.030



558  $\pm 0.005$ ), despite the different methods applied for the derivation of DOD and its uncertainty. Our  
559 global DOD long-term average is very close to the CALIOP derived value (0.029) and about half of  
560 the MODIS derived one (0.067) reported by Song et al. (2021).

561 Our continental ( $0.070 \pm 0.005$ ) and oceanic ( $0.019 \pm 0.002$ ) mean DODs (see Table 1) are  
562 substantially lower than those obtained in Voss and Evan (2020) (land: 0.1; ocean: 0.03). This  
563 difference may be attributed to the different averaging approaches, which can have an important  
564 impact on the calculations as it has been shown in Levy et al. (2009) (see their Figure 5). Based on  
565 our method, we are giving the same “weight” at each grid cell (regardless of the amount of available  
566 data in that grid cell throughout the study period) when we are calculating the domain (from regional  
567 to global) average. Therefore, we are avoiding an overestimation of the spatial average since MIDAS  
568 data availability is larger over/nearby deserts (see Figure 8-c in Gkikas et al. (2021)) where the higher  
569 DODs are observed. To be more specific, when we are calculating the global long-term DOD average  
570 based on the second branch (i.e., “Straight”, the standard approach for the calculation of the average  
571 value by considering all the available values in space and time) in Levy et al. (2009), we obtain a  
572 climatological value equal to 0.047. Such different approaches for the calculation of the long-term  
573 DOD averages might interpret and the deviations found between this study and Song et al. (2021).  
574 Finally, the computed global mean MIDAS DOD is somewhat higher than those simulated by most  
575 AeroCom Phase I models (Huneeus et al., 2011), being about 40% higher than the median (0.023);  
576 nevertheless, it must be taken into account that most models consider the diurnal variation of DOD  
577 in contrast to the single-measurements taken during MODIS overpass.

578 As expected, the interannual GLB DOD timeseries is driven by the variability in the NHE DOD  
579 (Figure 10 ii-a) since the most widespread and intense dust sources are located in the Northern  
580 Hemisphere. This is justified by their high temporal co-variation while a positive NHE-GLB offset is  
581 constantly observed, being lower during boreal winter and autumn (up to 0.035) and maximum during  
582 the high dust seasons (0.058). The fraction of monthly NHE AOD attributed to dust particles ranges  
583 from 20% to 48% and the  $R^2$  value between monthly AOD and DOD is equal to 0.94, both indicating  
584 a dominant dust contribution. Over the study period (2003-2017), the NHE DOD yields a  
585 climatological mean equal to  $0.056 \pm 0.004$  (Table 1) ranging from  $0.024 \pm 0.015$  (Dec 2005) to  $0.121$   
586  $\pm 0.050$  (Mar 2012). In contrast, marine and biomass burning aerosols, rather than dust, regulate AOD  
587 in the Southern Hemisphere (Figure 10 iii-a). SHE DODs are estimated to be low ( $0.008 \pm 0.001$ ),  
588 with the maximum value ( $0.016 \pm 0.016$ ) recorded in February 2016. The contribution of dust aerosols  
589 to the total aerosol load does not exceed 17% throughout the study period (Fig. 10 iii-a) and on  
590 average it is equal to  $8.2\% \pm 1.1\%$ , which is in very good agreement with the findings by Kok et al.  
591 (2021b).

592 A better view of the seasonal cycles of AOD, DOD and the DOD-to-AOD ratio can be obtained  
593 by investigating their climatological patterns, representative for the period of interest (2003-2017).  
594 On a global scale (Fig. 10 i-b), DODs peak between March and June (~0.045), and then decline until  
595 November (0.018) before rising during boreal winter. Despite the monthly shifts between maximum  
596 AOD and DOD averages, the seasonal cycles of the total aerosol and dust burdens are similar to a  
597 large extent, whereas the contribution of mineral particles to the total extinction ranges from 16%  
598 (November) to 33% (March-June). The MIDAS global DOD-to-AOD ratio (~23%) is close to the  
599 values reported by Gelaro et al. (2017) and Kinne et al. (2006), ~22% and ~26%, respectively, but  
600 higher than most of the model-derived estimations (12% - 28%) from the AeroCom Phase III (Gliss  
601 et al., 2021). These discrepancies, excluding the aerosol parametrizations, may be partly due to the  
602 different sampling between single-overpass satellite observations and reanalyses (Gelaro et al., 2017)  
603 or models (Kinne et al., 2006) where the diurnal aerosol variability (Schepanski et al., 2009; Yu et  
604 al., 2021) is included. In the NHE (Fig. 10 ii-b), the mean seasonal trend of DODs remains relatively  
605 unchanged when compared with GLB; however, the hemispheric means (0.030-0.088) and the dust  
606 fraction (24-41%) are higher. On the contrary, the weak signal of aeolian dust in SHE (Fig. 10 iii-b)  
607 interprets the very low DODs (0.005 – 0.011) and their minor impact (6-12%) upon AOD magnitude.

608 The analysis presented above has also been conducted for each one of the 17 sub-regions  
609 illustrated in Figure 7 in Gkikas et al. (2021), and the main findings are summarized in this paragraph.  
610 Among the regional domains, a persistency of high DODs (>0.3), both at interannual and seasonal  
611 scales, it is found only in BOD, which yields a long-term average value equal to  $0.533 \pm 0.009$ , being  
612 almost double than WSA ( $0.302 \pm 0.006$ ) and TAK ( $0.246 \pm 0.020$ ) as illustrated in Table 1. However,  
613 when focus is given to individual months, the maximum DODs over the study period (Fig. 11 vi-a)  
614 and on their climatological levels are recorded in the Taklamakan Desert and can be as high as 0.868  
615 (April 2007) and 0.600 (April), respectively. Comparable or even higher DODs than those computed  
616 in BOD, are also evident for specific months in THA (Fig. 11 vii-a), GOG (Fig. 11 xii-a) and SSA  
617 (Fig. 11 xv-a) as well as on the monthly timeseries (THA; Fig. 11 vii-b). Mineral particles'  
618 contribution to the total AOD (i.e., blue curves in the seasonal cycle plots) is at least 50% over dust  
619 sources or dust-abundant areas in N. Africa, Middle East and Asia and it is constantly higher than  
620 70%, reaching up to 95%, in BOD (Fig. 11 i-b), WSA (Fig. 11 viii-b) and TAK (Fig. 11 vi-b). Over  
621 downwind regions, such as EAS (Fig. 11 ix-b), GOG (Fig. 11 xii-b), MED (Fig. 11 xiii-b) and SSA  
622 (Fig. 11 xv-b), the dust contribution can prevail over the non-dust portion (GOG, MED, SSA) while  
623 in EAS does not exceed 30%, due to the predominance of anthropogenic aerosols. In the oceanic  
624 areas of Tropical Atlantic and North Pacific, where large-scale dust transport is taking place, AOD  
625 and DOD co-vary, indicating that the dust activity regulates the temporal variations of aerosols' load,  
626 except during summer months in WNP (Fig. 11 xvi-a, xvi-b). Regarding the seasonal cycle of DOD,

627 the maximum values are recorded either during boreal spring (GOB, CAS, NME, SUS, TAK, EAS,  
628 ENP, GOG, MED, WNP and SSA) or during boreal summer (THA, WSA, ETA, SME and WTA) or  
629 are similar between the two high-dust seasons (BOD).

630 A final intercomparison of the MIDAS DODs against those derived by Ridley et al. (2016) and  
631 Adebisi et al. (2020), on a seasonal basis over the period 2004 - 2008, has been performed for 15  
632 regions defined in Kok et al. (2021a) (see their Figure 2-b and Table 2). The obtained results are  
633 illustrated in Figure 12. For the southern hemisphere regions (Figs. 12 –xiii, xiv, xv) as well as for  
634 North America (Fig. 12-xii), MIDAS DODs are compared versus those from Adebisi et al. (2020)  
635 while for the remaining 11 domains (Figs. 12-i – xi) the results from Ridley et al. (2016) have been  
636 utilized. As an overview, it is noted that the seasonal cycle among the three databases is commonly  
637 reproduced, with a few exceptions (Mali-Niger, Kyzyl Kum, Southern Africa), whereas the DOD  
638 uncertainties (represented by the error bars) are comparable. Regarding the magnitudes, MIDAS  
639 DODs are mainly somewhat lower than those of Ridley et al. (2016) across the dust belt in contrast  
640 to the outflow region of the Mid-Atlantic (Fig. 12-i). The obtained differences are mainly attributed  
641 to the consideration of different models for accounting for the non-dust portion, the different  
642 treatment of AODs (bias correction vs. quality filtering), the different versions of MODIS retrievals  
643 (C006 vs C061), the consideration of multi-satellite observations instead of relying only on MODIS-  
644 Aqua retrievals as well as to the different spatial scales (coarse vs. fine). In relative terms, the largest  
645 deviations are found in the desert areas of the southern hemisphere where models struggle to represent  
646 adequately the dust sources and the emitted amounts of mineral particles, thus affecting the dust  
647 fraction ratio provided by MERRA-2.

648

## 649 **5. Summary and conclusions**

650

651 The current study presents a scientific exploitation of the MIDAS dataset (Gkikas et al., 2021),  
652 which provides columnar mid-visible (550 nm) dust optical depth (DOD) at fine spatial resolution  
653 ( $0.1^\circ \times 0.1^\circ$ ) and over a 15-year period (2003 – 2017). Taking advantage of the global coverage of  
654 the MIDAS DOD product, we analyzed the contribution of dust aerosols to AOD at various spatial  
655 and temporal scales. More specifically, we focused on 9 regions that account for the majority of the  
656 global dust budget, encompassing sources and downwind areas with the main dust transport  
657 pathways. Such regions comprise the deserts extending across the “dust belt”, North America,  
658 Australia, South Africa and South America as well as maritime areas (Tropical Atlantic Ocean,  
659 Mediterranean, North Pacific Ocean) receiving constantly large amounts of mineral particles from  
660 the nearby deserts. At a further step, the interannual and intra-annual timeseries of DODs along with

661 their contribution to the total aerosol load (AOD), were investigated at global, hemispherical and  
662 regional level.

663 According to our findings, the global long-term DOD average over the study period (2003-2017)  
664 is equal to  $0.032 \pm 0.003$ , yielding a strong contrast between the contributions from the northern  
665 ( $0.056 \pm 0.004$ ) and southern ( $0.008 \pm 0.001$ ) hemispheres. Our global estimations are almost identical  
666 with those given by Ridley et al. (2016) and the CALIOP-derived estimate of Song et al. (2021), in  
667 contrast to the MODIS-based average reported in the latter study. Nevertheless, when the global  
668 averages are calculated separately over land ( $0.070 \pm 0.005$ ) and ocean ( $0.019 \pm 0.002$ ), our results  
669 differ substantially than those found in Voss and Evan (2020), who reported continental and maritime  
670 DODs equal to 0.100 and 0.030, respectively. Such large deviations are attributed to the different  
671 applied methodologies and averaging procedures followed. Moreover, we find very good agreement,  
672 in terms of DOD magnitude and uncertainty, of the MIDAS seasonal DODs versus those of Ridley  
673 et al. (2016) and Adebisi et al. (2020) for 15 regions defined in Kok et al. (2021a). Considering that  
674 the long-term DOD averages can be utilized for constraining global dust in climate models, or can be  
675 used in several other applications, a detailed analysis is required for enlightening the factors resulting  
676 in disagreements among studies. Likewise, our computed global DOD average resides around the  
677 middle of the AeroCom (Huneeus et al., 2011) limits, being higher than the median (0.023) and mean  
678 (0.028). However, in the model-based calculations the diurnal variability is taken into account in  
679 contrast to the satellite-based estimations relying on single overpass measurements per day.

680 Regarding the dust contribution to the total aerosol optical depth, the DOD-to-AOD ratio from  
681 32% at N. Hemisphere drops down to 8% in S. Hemisphere while at global scale is about one quarter  
682 (23%). The contradiction found between the two hemispheres, both for DOD and dust fraction, is  
683 interpreted by the most pronounced dust activity recorded in the Bodélé Depression of the northern  
684 Lake Chad Basin (DODs up to  $\sim 1.2$ ), across the Sahel (DODs up to 0.8), in western parts of the  
685 Sahara Desert (DODs up to 0.6), in the eastern parts of the Arabian Peninsula (DODs up to  $\sim 1$ ), along  
686 the Indus river basin (DODs up to 0.8) and in the Taklamakan Desert (DODs up to  $\sim 1$ ). On the  
687 contrary, the weaker emission mechanisms triggering dust mobilization over the spatially limited  
688 sources of Patagonia, South Africa and interior arid areas of Australia do not favor the accumulation  
689 of mineral particles at large amounts (DODs up to 0.4 at local hotspots), even during high-dust  
690 seasons. Except for the Bodélé Depression, where the seasonal variability of the intense dust loads is  
691 relatively weak, in the other dust sources of the N. Hemisphere, DODs exhibit a strong seasonal cycle  
692 with maximum levels either during boreal spring or summer and minimum in boreal winter.

693 Over oceans, the main pathways of long-range dust transport are observed along the tropical  
694 Atlantic and the northern Pacific, revealing a remarkable variation, within the course of the year, in  
695 terms of intensity, latitudinal position and range. Saharan dust plumes, reaching the Caribbean Sea in

696 summer under the impact of the trade winds, are more abundant with respect to Asian dust, arriving  
697 at the western coasts of the United States in spring under the impact of midlatitude cyclones. Due to  
698 the convergence of the Shamal winds, blowing over the Arabian Peninsula, and the wind flow from  
699 the subtropical anticyclone, dust aerosols originating in the Middle East can reach the western Indian  
700 coasts in summer, crossing the Arabian Sea. Dust loads in the southern parts of the Red Sea are  
701 maximized during boreal summer when Saharan or Middle East dust is transported, depending on the  
702 zonal airflow. The intensity of dust burden in the Mediterranean forms a south-north gradient,  
703 whereas a seasonal longitudinal shift of the maximum DODs, off the northern African coasts, is  
704 evident attributed to the prevailing synoptic circulation.

705 Despite the strong capabilities of the MIDAS dataset, we have also identify some limitations,  
706 thoroughly discussed here and in Gkikas et al. (2021), attributed either to inherent weaknesses of the  
707 raw MODIS AOD retrievals or to deficiencies of MDF, resulting in not too realistic patterns in  
708 specific regions (e.g., South America, Gulf of Guinea, Aral Sea) of the planet. Thanks to this detailed  
709 analysis, potential users are aware of any issue that may rise when utilizing the MIDAS DOD product.

710 Concerning the DOD uncertainties presented here, in the MIDAS dataset, MODIS AOD  
711 retrievals, obtained based on different assumptions in the respective algorithms, and MERRA-2  
712 products are mixed. Therefore, the AOD and MDF errors, combined in the DOD uncertainty and  
713 carried through spatial and temporal averaging, are more likely heterogeneous and quite difficult to  
714 be quantified. Actually, the evaluation of spaceborne retrievals and numerical outputs can be much  
715 more complex and definitely further work is needed towards optimizing the confidence margins of  
716 total (speciated) optical depth levels. Quantifying accurately satellite based aerosol uncertainties is  
717 still an open issue and it is among our priorities to minimize the impacts of the aforementioned  
718 drawbacks and misrepresentations in the future versions of the MIDAS dataset.

719 As already mentioned, a variety of research studies can rely on the MIDAS dataset. MIDAS has  
720 been already used for the investigation of DOD trends (Logothetis et al., 2021) whereas in a follow-  
721 up study the mechanisms contributing to the temporal variations of dust burden will be investigated.  
722 Likewise, the MIDAS DOD product has been utilized in radiative transfer studies (Fountoulakis et  
723 al, 2021; Masoom et al., 2021) focusing on the impacts on solar energy production. Moreover, taking  
724 advantage of the fine spatial resolution of the MIDAS dataset and of its extended temporal  
725 availability, the dataset can be used for the identification of dust sources worldwide, similarly to the  
726 analysis done in Ginoux et al. (2012). Finally, we have provided a simple, yet flexible method  
727 (independent from other datasets) to calculate consistent uncertainties across spatiotemporal scales,  
728 which will ease the use of the MIDAS dataset in data assimilation applications.

729  
730

731 **Acknowledgments**

732 Antonis Gkikas acknowledges support by the Hellenic Foundation for Research and Innovation  
733 (H.F.R.I.) under the “2nd Call for H.F.R.I. Research Projects to support Post-Doctoral Researchers”  
734 (Project Acronym: ATLANTAS, Project Number: 544). Vassilis Amiridis acknowledges support  
735 from the European Research Council (grant no. 725698; D-TECT). Eleni Marinou was funded by a  
736 DLR VO-Ryoung investigator group and the Deutscher Akademischer Austauschdienst (grant no.  
737 57370121). Jasper F. Kok acknowledges support from National Science Foundation (NSF) grant  
738 1552519. Carlos Pérez García-Pando acknowledges support from the European Research Council  
739 (grant no. 773051; FRAGMENT), the AXA Research Fund, and the Spanish Ministry of Science,  
740 Innovation and Universities (grant nos. RYC-2015-18690 and CGL2017- 88911-R). The authors  
741 acknowledge support from the DustClim project as part of ERA4CS, an ERA-NET project initiated  
742 by JPI Climate and funded by FORMAS (SE), DLR (DE), BMWFV (AT), IFD (DK), MINECO  
743 (ES), and ANR (FR), with cofunding by the European Union (grant no. 690462). PRACE (Partnership  
744 for Advanced Computing in Europe) and RES (Red Española de Supercomputación) are  
745 acknowledged for awarding access to the MareNostrum Supercomputer in the Barcelona  
746 Supercomputing Center. We acknowledge support of this work by the PANhellenic infrastructure for  
747 Atmospheric Composition and climatE chAnge (PANACEA) project (grant no. MIS 5021516),  
748 which is implemented under the Horizon 2020 Action of “Reinforcement of the Research and  
749 Innovation Infrastructure”, funded by the Operational Programme Competitiveness,  
750 Entrepreneurship, and Innovation (NSRF 2014–2020) and cofinanced by Greece and the European  
751 Union (under the European Regional Development Fund). NOA members acknowledge support from  
752 the Stavros Niarchos Foundation (SNF). The authors acknowledge support by the COST Action  
753 “InDust” (grant no. CA16202), supported by COST (European Cooperation in Science and  
754 Technology). The authors would like to thank Andrew Mark Sayer for his valuable and constructive  
755 comments. The authors would like also to thank Thanasis Georgiou for developing the ftp server on  
756 which the MIDAS data set is stored.

757

758 **Data availability**

759

760 The MIDAS dataset has been developed in the framework of the DUST-GLASS project (grant no.  
761 749461; European Union’s Horizon 2020 Research and Innovation programme under the Marie  
762 Skłodowska-Curie Actions) and it is available at: <https://doi.org/10.5281/zenodo.4244106>.

763

764

765

766 **References**

767 Adebisi, A. A., Kok, J. F., Wang, Y., Ito, A., Ridley, D. A., Nabat, P., and Zhao, C.: Dust Constraints  
768 from joint Observational-Modelling-experiMental analysis (DustCOMM): comparison with  
769 measurements and model simulations, *Atmos. Chem. Phys.*, 20, 829–863,  
770 <https://doi.org/10.5194/acp-20-829-2020>, 2020.

771 Alam, K., Qureshi, S., & Blaschke, T.: Monitoring spatio-temporal aerosol patterns over Pakistan  
772 based on MODIS, TOMS and MISR satellite data and a HYSPLIT model. *Atmospheric Environment*,  
773 45, 4641–4651, 2011.

774 Alizadeh-Choobari, O., Zawar-Reza, P., Sturman, A.: The “wind of 120 days” and dust storm activity  
775 over the Sistan Basin, *Atmos. Res.*, 143, 328–341, 2014.

776  
777 Amiridis, V., Wandinger, U., Marinou, E., Giannakaki, E., Tsekeri, A., Basart, S., Kazadzis, S.,  
778 Gkikas, A., Taylor, M., Baldasano, J., and Ansmann, A.: Optimizing CALIPSO Saharan dust  
779 retrievals, *Atmos. Chem. Phys.*, 13, 12089–12106, <https://doi.org/10.5194/acp-13-12089-2013>, 2013.

780  
781 Amiridis, V., Marinou, E., Tsekeri, A., Wandinger, U., Schwarz, A., Giannakaki, E., Mamouri, R.,  
782 Kokkalis, P., Biniotoglou, I., Solomos, S., Herekakis, T., Kazadzis, S., Gerasopoulos, E., Proestakis,  
783 E., Kottas, M., Balis, D., Papayannis, A., Kontoes, C., Kourtidis, K., Papagiannopoulos, N., Mona,  
784 L., Pappalardo, G., Le Rille, O., and Ansmann, A.: LIVAS: a 3-D multi-wavelength aerosol/cloud  
785 database based on CALIPSO and EARLINET, *Atmos. Chem. Phys.*, 15, 7127–7153,  
786 <https://doi.org/10.5194/acp-15-7127-2015>, 2015.

787  
788 Baddock, M. C., Ginoux, P., Bullard, J. E., and Gill, T. E.: Do MODIS-defined dust sources have a  
789 geomorphological signature?, *Geophys. Res. Lett.*, 43, GL067327, doi:10.1002/2015GL067327,  
790 2016.

791  
792 Banks, J. R., Brindley, H. E., Stenchikov, G., and Schepanski, K.: Satellite retrievals of dust aerosol  
793 over the Red Sea and the Persian Gulf (2005–2015), *Atmos. Chem. Phys.*, 17, 3987–4003,  
794 <https://doi.org/10.5194/acp-17-3987-2017>, 2017.

795  
796 Basile, I., Grousset, F. E., Revel, M., Petit, J.-R., Biscaye, P. E., and Barkov, N. I.: Patagonian origin  
797 of glacial dust deposited in East Antarctica (Vostok and Dome C) during glacial stages 2, 4 and 6,  
798 *Earth Planet. Sc. Lett.*, 146, 573–589, 1997.

799

800 Brindley, H., Osipov, S., Bantges, R., Smirnov, A., Banks, J., Levy, R., Jish Prakash, P., and  
801 Stenchikov, G.: An assessment of the quality of aerosol retrievals over the Red Sea and evaluation of  
802 the climatological cloud-free dust direct radiative effect in the region, *J. Geophys. Res.-Atmos.*, 120,  
803 10862–10878, doi:10.1002/2015JD023282, 2015.

804

805 Bryant, R. G., Bigg, G. R., Mahowald, N. M., Eckardt, F. D., and Ross S. G.: Dust emission response  
806 to climate in southern Africa, *J. Geophys. Res.*, 112, D09207, doi:10.1029/2005JD007025, 2007.

807

808 Bullard, J. E., and Austin, M. J.: Dust generation on a proglacial floodplain, West Greenland. *Aeolian*  
809 *Res.* 3, 43–54. doi: 10.1016/j.aeolia.2011.01.002, 2011, 2017.

810

811 Bullard, J. E., Baddock, M., Bradwell, T., Crusius, J., Darlington, E., Gaiero, D., Gassó, S.,  
812 Gisladottir, G., Hodgkins, R., McCulloch, R., McKenna-Neuman, C., Mockford, T., Stewart, H., and,  
813 Thorsteinsson, T.: High-latitude dust in the Earth system, *Rev. Geophys.*, 54, 447–485,  
814 <https://doi.org/10.1002/2016RG000518>, 2016.

815

816 Bullard, J., Baddock, M., McTainsh, G. H., and Leys, J. F.: Subbasin scale dust source  
817 geomorphology detected using MODIS, *Geophys. Res. Lett.*, 35, L15404,  
818 doi:10.1029/2008GL033928, 2008.

819 Chin, M., Ginoux, P., Kinne, S., Torres, O., Holben, B. N., Duncan, D. N., Martin, R. V., Logan, J.  
820 A., Higurashi, H., and Nakajima, T.: Tropospheric aerosol optical thickness from the GOCART  
821 model and comparisons with satellite and Sun photometer measurements, *J. Atmos. Sci.*, 59, 451–  
822 483, [https://doi.org/10.1175/1520-0469\(2002\)059<0461:TAOTFT>2.0.CO;2](https://doi.org/10.1175/1520-0469(2002)059<0461:TAOTFT>2.0.CO;2), 2002.

823

824 de Leeuw, G., Sogacheva, L., Rodriguez, E., Kourtidis, K., Georgoulas, A. K., Alexandri, G.,  
825 Amiridis, V., Proestakis, E., Marinou, E., Xue, Y., and van der A, R.: Two decades of satellite  
826 observations of AOD over mainland China using ATSR-2, AATSR and MODIS/Terra: data set  
827 evaluation and large-scale patterns, *Atmos. Chem. Phys.*, 18, 1573-1592, [https://doi.org/10.5194/acp-](https://doi.org/10.5194/acp-18-1573-2018)  
828 [18-1573-2018](https://doi.org/10.5194/acp-18-1573-2018), 2018.

829

830 Dey, S. and Di Girolamo, L.: A climatology of aerosol optical and microphysical properties over the  
831 Indian subcontinent from 9 years (2000–2008) of Multiangle Imaging Spectroradiometer (MISR)  
832 data, *J. Geophys. Res.-Atmos.*, 115, D15204, <https://doi.org/10.1029/2009JD013395>, 2010.

833



834 Dey, S., Tripathi, S. N., Singh, R. P., and Holben, B. N.: Influence of dust storms on the aerosol  
835 optical properties over the Indo-Gangetic basin, *J. Geophys. Res.-Atmos.*, 109, 1–10,  
836 doi:10.1029/2004jd004924, 2004.

837

838 Di Tomaso, E., Schutgens, N. A. J., Jorba, O., and Pérez García-Pando, C.: Assimilation of MODIS  
839 Dark Target and Deep Blue observations in the dust aerosol component of NMMB-MONARCH  
840 version 1.0, *Geosci. Model Dev.*, 10, 1107–1129, <https://doi.org/10.5194/gmd-10-1107-2017>, 2017.

841

842 Doherty, O. M., Riemer, N., and Hameed, S.: Control of Saharan mineral dust transport to Barbados  
843 in winter by the Intertropical Convergence Zone over West Africa: Winter dust in Barbados and the  
844 ITCZ, *J. Geophys. Res.-Atmos.*, 117, D19117, doi:10.1029/2012JD017767, 2012.

845

846 Du, Y., Xu, X., Chu, M., Guo, Y., and Wang, J.: Air particulate matter and cardiovascular disease:  
847 the epidemiological, biomedical and clinical evidence, *J. Thorac. Dis.*, 8, E8,  
848 <https://doi.org/10.3978/j.issn.2072-1439.2015.11.37>, 2016.

849

850 Eck, T. F., Holben, B. N., Sinyuk, A., Pinker, R. T., Goloub, P., Chen, H., Chatenet, B., Li, Z., Singh,  
851 R. P., and Tripathi, S. N.: Climatological aspects of the optical properties of fine/coarse mode aerosol  
852 mixtures, *J. Geophys. Res.-Atmos.*, 115, 19205, <https://doi.org/10.1029/2010JD014002>, 2010.

853

854 Eckardt, F.D. Kuring, N.: SeaWiFS identifies dust sources in the Namib Desert. *International Journal*  
855 *of Remote Sensing*, 26:4159–4167, 2005.

856

857 Eguchi, K., Uno, I., Yumimoto, K., Takemura, T., Shimizu, A., Sugimoto, N., and Liu, Z.: Trans-  
858 pacific dust transport: integrated analysis of NASA/CALIPSO and a global aerosol transport model,  
859 *Atmos. Chem. Phys.*, 9, 3137–3145, <https://doi.org/10.5194/acp-9-3137-2009>, 2009.

860

861 Elguindi, N., Solmon, F., Turuncoglu, U.: Quantifying some of the impacts of dust and other aerosol  
862 on the Caspian Sea region using a regional climate model. *Clim. Dyn.*, 46, 41–55, 2016.

863

864 Fiedler, S., Schepanski, K., Heinold, B., Knippertz, P., and Tegen, I.: Climatology of nocturnal low-  
865 level jets over North Africa and implications for modeling mineral dust emission, *J. Geophys. Res.-*  
866 *Atmos.*, 118, 6100–6121, 2013.

867

868 Flaounas, E., Kotroni, V., Lagouvardos, K., Kazadzis, S., Gkikas, A., and Hatzianastassiou, N.:  
869 Cyclone contribution to dust transport over the Mediterranean region, *Atmos. Sci. Lett.*, 16, 473–478,  
870 doi:10.1002/asl.584, 2015.

871

872 Foth, A., Kanitz, T., Engelmann, R., Baars, H., Radenz, M., Seifert, P., Barja, B., Fromm, M.,  
873 Kalesse, H., and Ansmann, A.: Vertical aerosol distribution in the southern hemispheric midlatitudes  
874 as observed with lidar in Punta Arenas, Chile (53.2° S and 70.9° W), during ALPACA, *Atmos. Chem.*  
875 *Phys.*, 19, 6217–6233, <https://doi.org/10.5194/acp-19-6217-2019>, 2019.

876

877 Fountoulakis, Ilias, Panagiotis Kosmopoulos, Kyriakoula Papachristopoulou, Ioannis-Panagiotis  
878 Raptis, Rodanthi-Elisavet Mamouri, Argyro Nisantzi, Antonis Gkikas, Jonas Witthuhn, Sebastian  
879 Bley, Anna Moustaka, Johannes Buehl, Patric Seifert, Diofantos G. Hadjimitsis, Charalampos  
880 Kontoes, and Stelios Kazadzis. 2021. "Effects of Aerosols and Clouds on the Levels of Surface Solar  
881 Radiation and Solar Energy in Cyprus" *Remote Sensing* 13, no. 12: 2319.  
882 <https://doi.org/10.3390/rs13122319>

883

884 Gassó, S., Stein, A., Marino, F., Castellano, E., Udisti, R., and Ceratto, J.: A combined observational  
885 and modeling approach to study modern dust transport from the Patagonia desert to East Antarctica,  
886 *Atmos. Chem. Phys.*, 10, 8287–8303, <https://doi.org/10.5194/acp-10-8287-2010>, 2010.

887

888 Gassó, S., & Torres, O.: Temporal characterization of dust activity in the Central Patagonia desert  
889 (years 1964–2017), *Journal of Geophysical Research: Atmospheres*, 124, 3417– 3434,  
890 <https://doi.org/10.1029/2018JD030209>, 2019.

891

892 Ge, J. M., Huang, J. P., Xu, C. P., Qi, Y. L., and Liu, H. Y.: Characteristics of Taklimakan dust  
893 emission and distribution: a satellite and reanalysis field perspective, *J. Geophys. Res.-Atmos.*, 119,  
894 11772–11783, <https://doi.org/10.1002/2014JD022280>, 2014.

895

896 Gelaro, R, McCarty, W., Suárez, M. J., Todling, R., Molod, A., Takacs, L., Randles, C. A., Darmenov,  
897 A., Bosilovich, M. G., Reichle, R., Wargan, K., Coy, L., Cullather, R., Draper, C., Akella, S.,  
898 Buchard, V., Conaty, A., da Silva, A. M., Gu, W., Kim, G., Koster, R., Lucchesi, R., Merkova, D.,  
899 Nielsen, J. E., Partyka, G., Pawson, S., Putman, W., Rienecker, M., Schubert, S. D., Sienkiewicz, M.,  
900 and Zhao, B.: The Modern-Era Retrospective Analysis for Research and Applications, Version 2  
901 (MERRA-2), *J. Climate*, 30, 5419–5454, <https://doi.org/10.1175/JCLI-D-16-0758.1>, 2017.

902

903 Gill, T. E.: Eolian sediments generated by anthropogenic disturbance of playas: human impacts on  
904 the geomorphic system and geomorphic impacts on the human system, *Geomorphology*, 17, 207–  
905 228, 1996.

906

907 Ginoux, P., Prospero, J. M., Torres, O., and Chin, M.: Longterm simulation of global dust distribution  
908 with the GOCART model: correlation with North Atlantic Oscillation, *Environ. Modell. Softw.*, 19,  
909 113–128, [https://doi.org/10.1016/S1364-8152\(03\)00114-2](https://doi.org/10.1016/S1364-8152(03)00114-2), 2004.

910

911 Ginoux, P., Prospero, J. M., Gill, T. E., Hsu, N. C., and Zhao, M.: Global-scale attribution of  
912 anthropogenic and natural dust sources and their emission rates based on MODIS Deep Blue aerosol  
913 products, *Rev. Geophys.*, 50, RG3005, <https://doi.org/10.1029/2012RG000388>, 2012.

914

915 Gkikas, A., Hatzianastassiou, N., Mihalopoulos, N., Katsoulis, V., Kazadzis, S., Pey, J., Querol, X.,  
916 and Torres, O.: The regime of intense desert dust episodes in the Mediterranean based on  
917 contemporary satellite observations and ground measurements, *Atmos. Chem. Phys.*, 13, 12135–  
918 12154, <https://doi.org/10.5194/acp-13-12135-2013>, 2013.

919

920 Gkikas, A., Houssos, E. E., Lolis, C. J., Bartzokas, A., Mihalopoulos, N., and Hatzianastassiou, N.:  
921 Atmospheric circulation evolution related to desert-dust episodes over the Mediterranean, *Q. J. Roy.  
922 Meteor. Soc.*, 141, 1634–1645, doi:10.1002/qj.2466, 2015.

923

924 Gkikas, A., Basart, S., Hatzianastassiou, N., Marinou, E., Amiridis, V., Kazadzis, S., Pey, J., Querol,  
925 X., Jorba, O., Gassó, S., and Baldasano, J. M.: Mediterranean intense desert dust outbreaks and their  
926 vertical structure based on remote sensing data, *Atmos. Chem. Phys.*, 16, 8609–8642,  
927 <https://doi.org/10.5194/acp-16-8609-2016>, 2016.

928

929 Gkikas, A., Obiso, V., Pérez García-Pando, C., Jorba, O., Hatzianastassiou, N., Vendrell, L., Basart,  
930 S., Solomos, S., Gassó, S., and Baldasano, J. M.: Direct radiative effects during intense Mediterranean  
931 desert dust outbreaks, *Atmos. Chem. Phys.*, 18, 8757–8787, [https://doi.org/10.5194/acp-18-8757-](https://doi.org/10.5194/acp-18-8757-2018)  
932 2018, 2018.

933

934 Gkikas, A., Giannaros, T.M., Kotroni, V., Lagouvardos, K.: Assessing the radiative impacts of an  
935 extreme desert dust outbreak and the potential improvements on short-term weather forecasts: The  
936 case of February 2015, *Atmos. Res.*, 226, 152–170, <https://doi.org/10.1016/j.atmosres.2019.04.020>,  
937 2019.

938

939 Gkikas, A., Proestakis, E., Amiridis, V., Kazadzis, S., Di Tomaso, E., Tsekeri, A., Marinou, E.,  
940 Hatzianastassiou, N., and Pérez García-Pando, C.: ModIs Dust AeroSol (MIDAS): a global fine-  
941 resolution dust optical depth data set, *Atmos. Meas. Tech.*, 14, 309–334, [https://doi.org/10.5194/amt-](https://doi.org/10.5194/amt-14-309-2021)  
942 14-309-2021, 2021.

943

944 Gliß, J., Mortier, A., Schulz, M., Andrews, E., Balkanski, Y., Bauer, S. E., Benedictow, A. M. K.,  
945 Bian, H., Checa-Garcia, R., Chin, M., Ginoux, P., Griesfeller, J. J., Heckel, A., Kipling, Z., Kirkevåg,  
946 A., Kokkola, H., Laj, P., Le Sager, P., Lund, M. T., Lund Myhre, C., Matsui, H., Myhre, G., Neubauer,  
947 D., van Noije, T., North, P., Olivié, D. J. L., Rémy, S., Sogacheva, L., Takemura, T., Tsigaridis, K.,  
948 and Tsyro, S. G.: AeroCom phase III multi-model evaluation of the aerosol life cycle and optical  
949 properties using ground- and space-based remote sensing as well as surface in situ observations,  
950 *Atmos. Chem. Phys.*, 21, 87–128, <https://doi.org/10.5194/acp-21-87-2021>, 2021.

951

952 Hamidi, M., Kavianpour, M. R., and Shao, Y.: Synoptic analysis of dust storms in the Middle East,  
953 *Asia-Pac. J. Atmos. Sci.*, 49, 279–286, 2013.

954

955 Hand, J. L., Gill, T. E., and Schichtel, B. A.: Spatial and seasonal variability in fine mineral dust and  
956 coarse aerosol mass at re-mote sites across the United States, *J. Geophys. Res.-Atmos.*, 122, 3080–  
957 3097, <https://doi.org/10.1002/2016jd026290>, 2017.

958

959 Haywood, J. and Boucher, O.: Estimates of the direct and indirect radiative forcing due to  
960 tropospheric aerosols: A review, *Rev. Geophys.*, 38, 513–543,  
961 <https://doi.org/10.1029/1999RG000078>, 2000.

962

963 Huang, J., Lin, B., Minnis, P., Wang, T., Wang, X., Hu, Y., Yi, Y., and Ayers, J. K.: Satellite-based  
964 assessment of possible dust aerosols semi-direct effect on cloud water path over East Asia, *Geophys.*  
965 *Res. Lett.*, 33, L19802, <https://doi.org/10.1029/2006GL026561>, 2006.

966

967 Huneus, N., Schulz, M., Balkanski, Y., Griesfeller, J., Prospero, J., Kinne, S., Bauer, S., Boucher,  
968 O., Chin, M., Dentener, F., Diehl, T., Easter, R., Fillmore, D., Ghan, S., Ginoux, P., Grini, A.,  
969 Horowitz, L., Koch, D., Krol, M. C., Landing, W., Liu, X., Mahowald, N., Miller, R., Morcrette, J.-  
970 J., Myhre, G., Penner, J., Perlwitz, J., Stier, P., Takemura, T., and Zender, C. S.: Global dust model  
971 intercomparison in AeroCom phase I, *Atmos. Chem. Phys.*, 11, 7781–7816,  
972 <https://doi.org/10.5194/acp-11-7781-2011>, 2011.

973  
974 Husar, R. B., Tratt, D. M., Schichtel, D. M., Falke, S. R., Li, F., Jaffe, D., Gassó, S., Gill, T.,  
975 Laulainen, N. S., Lu, F., Reheis, M. C., Chun, Y., Westphal, D., Holben, B. N., Gueymard, C., McK-  
976 endry, I., Kuring, N., Feldman, G. C., McClain, C., Frouin, R. J., Merrill, J., DuBois, D., Vignola, F.,  
977 Murayama, T., Nickovic, S., Wilson, W. E., Sassen, K., Sugimoto, N., and Malm, W. C.: Asian dust  
978 events of April 1998, *J. Geophys. Res.*, 106, 18317–18330, <https://doi.org/10.1029/2000JD900788>,  
979 2001.

980

981 Ignatov, A. and Stowe, L.: Physical Basis, Premises, and SelfConsistency Checks of Aerosol  
982 Retrievals from TRMM VIRS, *J. Appl. Meteor.*, 39, 2259–2277, [https://doi.org/10.1175/1520-0450\(2001\)040<2259:PBPASC>2.0.CO;2](https://doi.org/10.1175/1520-0450(2001)040<2259:PBPASC>2.0.CO;2), 2000.

983

984

985 Indoitu, R., Kozhoridze, G., Batyrbaeva, M., Vitkovskaya, I., Orlovsky, N., Blumberg, D., Orlovsky,  
986 L.: Dust emission and environmental changes in the dried bottom of the Aral Sea. *Aeolian. Res.* 17,  
987 101–115, 2015, <https://doi.org/10.1016/j.aeolia.2015.02.004>.

988

989 Jickells, T. D., An, Z. S., Andersen, K. K., Baker, A. R., Bergametti, G., Brooks, N., Cao, J. J., Boyd,  
990 P. W., Duce, R. A., Hunter, K. A., Kawahata, H., Kubilay, N., laRoche, J., Liss, P. S., Mahowald, N.,  
991 Prospero, J. M., Ridgwell, A. J., Tegen, I., and Torres, R.: Global iron connections between desert  
992 dust, ocean biogeochemistry, and climate, *Science*, 308, 67–71, 2005.

993

994 Jickells, T., Boyd, P., and Hunter, K.: Biogeochemical impacts of dust on the global carbon cycle, in:  
995 *Mineral Dust*, edited by: Knippertz, P. and Stuut, J.-B. W., Springer, the Netherlands, 359–384, 2014.

996

997 Jin, Q., Wei, J., Pu, B., Yang, Z.-L., and Parajuli, S. P.: High summertime aerosol loadings over the  
998 Arabian Sea and their transport pathways. *Journal of Geophysical Research: Atmospheres*, 123, 10,568–10,590, <https://doi.org/10.1029/2018JD028588>, 2018.

1000

1001 Johnson, M. S., Meskhidze, N., Kiliyanpilakkil, V. P., and Gassó, S.: Understanding the transport of  
1002 Patagonian dust and its influence on marine biological activity in the South Atlantic Ocean, *Atmos.*  
1003 *Chem. Phys.*, 11, 2487–2502, <https://doi.org/10.5194/acp-11-2487-2011>, 2011.

1004

1005 Kanakidou, M., Mihalopoulos, N., Kindap, T., Im, U., Vrekoussis, M., Gerasopoulos, E., Dermitzaki,  
1006 E., Unal, A., Kocak, M., Markakis, K., Melas, D., Kouvarakis, G., Youssef, A. F., Richter, A.,  
1007 Hatzianastassiou, N., Hilboll, A., Ebojie, F., Wittrock, F., von Savigny, C., Burrows, J. P.,

1008 Ladstaetter-Weissenmayer, A., and Moubasher, H.: Megacities as hot spots of air pollution in the  
1009 East Mediterranean, *Atmos. Environ.*, 45, 1223–1235,  
1010 <https://doi.org/10.1016/j.atmosenv.2010.11.048>, 2011.  
1011

1012 Kanatani, K.T., Ito, I., Al-Delaimy, W.K., Adachi, Y., Mathews, W.C., Ramsdell, J.W.: Toyama  
1013 Asian Desert Dust and Asthma Study Group Members. Desert dust exposure is associated with  
1014 increased risk of asthma hospitalization in children, *Am. J. Respir. Crit. Care Med.* 182 (12),  
1015 1475e1481. <https://doi.org/10.1164/rccm.201002-0296OC>, 2010.  
1016

1017 Kinne, S., Schulz, M., Textor, C., Guibert, S., Balkanski, Y., Bauer, S. E., Berntsen, T., Berglen, T.  
1018 F., Boucher, O., Chin, M., Collins, W., Dentener, F., Diehl, T., Easter, R., Feichter, J., Fillmore, D.,  
1019 Ghan, S., Ginoux, P., Gong, S., Grini, A., Hendricks, J., Herzog, M., Horowitz, L., Isaksen, I., Iversen,  
1020 T., Kirkevåg, A., Kloster, S., Koch, D., Kristjansson, J. E., Krol, M., Lauer, A., Lamarque, J. F.,  
1021 Lesins, G., Liu, X., Lohmann, U., Montanaro, V., Myhre, G., Penner, J., Pitari, G., Reddy, S., Seland,  
1022 O., Stier, P., Takemura, T., and Tie, X.: An AeroCom initial assessment – optical properties in aerosol  
1023 component modules of global models, *Atmos. Chem. Phys.*, 6, 1815-1834,  
1024 <https://doi.org/10.5194/acp-6-1815-2006>, 2006.  
1025

1026 Klose, M., Shao, Y., Karremann, M. K., and Fink, A.: Sahel dust zone and synoptic background,  
1027 *Geophys. Res. Lett.*, 37, L09802, <https://doi.org/10.1029/2010GL042816>, 2010.  
1028

1029 Knight, A. W., McTainsh, G. H., & Simpson, R. W.: Sediment loads in an Australian dust storm—  
1030 Implications for present and past dust processes. *Catena*, 24(3), 195–213,  
1031 [https://doi.org/10.1016/0341-8162\(95\)00026-O](https://doi.org/10.1016/0341-8162(95)00026-O), 1995.  
1032

1033 Knippertz, P., Deutscher, C., Kandler, K., Müller, T., Schulz, O., and Schütz, L.: Dust mobilization  
1034 due to density currents in the Atlas region: Observations from the Saharan Mineral Dust Experiment  
1035 2006 field campaign, *J. Geophys. Res.-Atmos.*, 112, 1–14, <https://doi.org/10.1029/2007JD008774>,  
1036 2007.  
1037

1038 Knippertz, P., Evans, M., Field, P. R., Fink, A. H., Liousse, C., and Marsham, J. H.: The possible role  
1039 of local air pollution in climate change in West Africa, *Nat. Clim. Chang.*, 5, 815–822,  
1040 <https://doi.org/10.1038/NCLIMATE2727>, 2015.  
1041

1042 Knippertz, P. and Todd, M. C.: Mineral Dust Aerosols over the Sahara: Meteorological Controls on  
1043 Emission and Transport and Implications for Modeling, *Rev. Geophys.*, 50, RG1007,  
1044 <https://doi.org/10.1029/2011RG000362>, 2012.

1045

1046 Koch, J. and Renno, N. O.: The role of convective plumes and vortices on the global aerosol budget,  
1047 *Geophys. Res. Lett.*, 32, L18806, doi:10.1029/2005GL023420, 2005.

1048

1049 Kok, J. F., Adebisi, A. A., Albani, S., Balkanski, Y., Checa-Garcia, R., Chin, M., Colarco, P. R.,  
1050 Hamilton, D. S., Huang, Y., Ito, A., Klose, M., Leung, D. M., Li, L., Mahowald, N. M., Miller, R. L.,  
1051 Obiso, V., Pérez García-Pando, C., Rocha-Lima, A., Wan, J. S., and Whicker, C. A.: Improved  
1052 representation of the global dust cycle using observational constraints on dust properties and  
1053 abundance, *Atmos. Chem. Phys.*, 21, 8127–8167, <https://doi.org/10.5194/acp-21-8127-2021>, 2021a.

1054

1055 Kok, J. F., Adebisi, A. A., Albani, S., Balkanski, Y., Checa-Garcia, R., Chin, M., Colarco, P. R.,  
1056 Hamilton, D. S., Huang, Y., Ito, A., Klose, M., Li, L., Mahowald, N. M., Miller, R. L., Obiso, V.,  
1057 Pérez García-Pando, C., Rocha-Lima, A., and Wan, J. S.: Contribution of the world's main dust source  
1058 regions to the global cycle of desert dust, *Atmos. Chem. Phys.*, 21, 8169–8193,  
1059 <https://doi.org/10.5194/acp-21-8169-2021>, 2021b.

1060

1061 Koren, I., Yoram, J. K., Richard, W., Martin, C. T., Yinon, R., Martins, J. V., and Daniel, R.: The  
1062 Bodélé depression: a single spot in the Sahara that provides most of the mineral dust to the Amazon  
1063 forest, *Environ. Res. Lett.*, 1, 014005, <https://doi.org/10.1088/1748-9326/1/1/014005>, 2006.

1064

1065 Kosmopoulos, P.G., Kazadzis, S., El-Askary, H., Taylor, M., Gkikas, A., Proestakis, E., Kontoes, C.,  
1066 El-Khayat, M.M.: Earth-Observation-Based Estimation and Forecasting of Particulate Matter Impact  
1067 on Solar Energy in Egypt, *Remote Sens.*, 10, 1870, 2018.

1068

1069 Lambert, F., Kug, J.-S., Park, R. J., Mahowald, N., Winckler, G., Abe-Ouchi, A., O'ishi, R.,  
1070 Takemura, T., and Lee, J.-H.: The role of mineral-dust aerosols in polar temperature amplification,  
1071 *Nat. Clim. Change*, 3, 487–491, <https://doi.org/10.1038/nclimate1785>, 2013.

1072

1073 Levy, R. C., Leptoukh, G. G., Kahn, R., Zubko, V., Gopalan, A., and Remer, L. A.: A critical look at  
1074 deriving monthly aerosol optical depth from satellite data, *IEEE T. Geosci. Remote*, 47, 2942–2956,  
1075 <https://doi.org/10.1109/TGRS.2009.2013842>, 2009.

1076

1077 Levy, R. C., Mattoo, S., Munchak, L. A., Remer, L. A., Sayer, A. M., Patadia, F., and Hsu, N. C.:  
1078 The Collection 6 MODIS aerosol products over land and ocean, *Atmos. Meas. Tech.*, 6, 2989–3034,  
1079 <https://doi.org/10.5194/amt-6-2989-2013>, 2013.

1080

1081 Li, L., and Sokolik, I.: Analysis of Dust Aerosol Retrievals Using Satellite Data in Central Asia,  
1082 *Atmosphere*, 9, 288, 2018.

1083

1084 Liu, D., Wang, Z., Liu, Z., Winker, D., and Trepte, C.: A height resolved global view of dust aerosols  
1085 from the first year CALIPSO lidar measurements, *J. Geophys. Res.-Atmos.*, 113, D16214,  
1086 <https://doi.org/10.1029/2007JD009776>, 2008.

1087

1088 Logothetis, S.-A., Salamalikis, V., Gkikas, A., Kazadzis, S., Amiridis, V., and Kazantzidis, A.: 15-  
1089 year variability of desert dust optical depth on global and regional scales, *Atmos. Chem. Phys.*, 21,  
1090 16499–16529, <https://doi.org/10.5194/acp-21-16499-2021>, 2021.

1091

1092 Mahowald, N. M. and Luo, C.: A less dusty future?, *Geophys. Res.Lett.*, 30, 1903,  
1093 <https://doi.org/10.1029/2003GL017880>, 2003.

1094

1095 Marinou, E., Amiridis, V., Biniotoglou, I., Tsikerdekis, A., Solomos, S., Proestakis, E., Konsta, D.,  
1096 Papagiannopoulos, N., Tsekeri, A., Vlastou, G., Zanis, P., Balis, D., Wandinger, U., and Ansmann,  
1097 A.: Three-dimensional evolution of Saharan dust transport towards Europe based on a 9-year  
1098 EARLINET-optimized CALIPSO dataset, *Atmos. Chem. Phys.*, 17, 5893-5919,  
1099 <https://doi.org/10.5194/acp-17-5893-2017>, 2017.

1100

1101 Marticoréna, B.: Mineral Dust - A key player in the Earth system, chap. Chapter 5: Dust production  
1102 mechanisms, pp. 93–120, Springer, 2014.

1103

1104 Masoom, A., Kosmopoulos, P., Bansal, A., Gkikas, A., Proestakis, E., Kazadzis, S., Amiridis, V.:  
1105 Forecasting dust impact on solar energy using remote sensing and modeling techniques, *Solar Energy*,  
1106 Vol. 228, 317-332, <https://doi.org/10.1016/j.solener.2021.09.033>, 2021.

1107

1108 Mazzonia, E., & Vazquez, M.: Desertification in Patagonia. In E. M. Latrubesse (Ed.), *Natural*  
1109 *hazards and human-exacerbated disasters in Latin America*, (Vol. 13, pp. 351–377). Elsevier,  
1110 [https://doi.org/https://doi.org/10.1016/S0928-2025\(08\)10017-7](https://doi.org/https://doi.org/10.1016/S0928-2025(08)10017-7), 2009.

1111



1112 McConnell, J. R., Aristarain, A. J., Banta, J. R., Edwards, P. R., and Simões, J. C.: 20th-century  
1113 doubling in dust archived in an Antarctic Peninsula ice core parallels climate change and  
1114 desertification in South America, *Proc. Natl. Acad. Sci. U. S. A.*, 104, 5743–5748, 2007.  
1115

1116 Micklin, P.: The Aral Sea disaster, *Annu. Rev. Earth Planet. Sci.*, 35, 47–72, 2007.  
1117

1118 Middleton, N. J.: Dust storms in the Middle East, *J. Arid Environ.*, 10, 83–96, 1986.  
1119

1120 Middleton, H. J.: Desert dust hazards: A global review, *Aeolian Res.*, 24, 53–63, 2017.  
1121

1122 Middleton, N. J. and Goudie, A. S.: Saharan dust: sources and trajectories, *T. I. Brit. Geogr.*, 26, 165–  
1123 181, doi:10.1111/1475- 5661.00013, 2001.  
1124

1125 Middleton, N.J., Kang, U.: Sand and dust storms: impact mitigation, *Sustainability*, 9, 1053,  
1126 <https://doi.org/10.3390/su9061053>, 2017.

1127 Mitchell, R. M., Forgan, B. W., and Campbell, S. K.: The Climatology of Australian Aerosol, *Atmos.*  
1128 *Chem. Phys.*, 17, 5131-5154, <https://doi.org/10.5194/acp-17-5131-2017>, 2017.

1129 Moran-Zuloaga, D., Ditas, F., Walter, D., Saturno, J., Brito, J., Carbone, S., Chi, X., Hrabě de  
1130 Angelis, I., Baars, H., Godoi, R. H. M., Heese, B., Holanda, B. A., Lavrič, J. V., Martin, S. T., Ming,  
1131 J., Pöhlker, M. L., Ruckteschler, N., Su, H., Wang, Y., Wang, Q., Wang, Z., Weber, B., Wolff, S.,  
1132 Artaxo, P., Pöschl, U., Andreae, M. O., and Pöhlker, C.: Long-term study on coarse mode aerosols in  
1133 the Amazon rain forest with the frequent intrusion of Saharan dust plumes, *Atmos. Chem. Phys.*, 18,  
1134 10055-10088, <https://doi.org/10.5194/acp-18-10055-2018>, 2018.  
1135

1136 Nabat, P., Somot, S., Mallet, M., Michou, M., Sevault, F., Driouech, F., Meloni, D., di Sarra, A., Di  
1137 Biagio, C., Formenti, P., Sicard, M., Léon, J.-F., and Bouin, M.-N.: Dust aerosol radiative effects  
1138 during summer 2012 simulated with a coupled regional aerosol–atmosphere–ocean model over the  
1139 Mediterranean, *Atmos. Chem. Phys.*, 15, 3303-3326, <https://doi.org/10.5194/acp-15-3303-2015>,  
1140 2015.  
1141

1142 Okin, G. S., Mahowald, N., Chadwick, O. A., and Artaxo, P.: Impact of desert dust on the  
1143 biogeochemistry of phosphorus in terrestrial ecosystems, *Global Biogeochem. Cy.*, 18, GB2005,  
1144 <https://doi.org/10.1029/2003GB002145>, 2004.  
1145

1146 O'Neill, N. T., Ignatov, A., Holben, B. N., and Eck, T. F.: The lognormal distribution as a reference  
1147 for reporting aerosol optical depth statistics; Empirical tests using multi-year, multi-site AERONET  
1148 Sunphotometer data, *Geophys. Res. Lett.*, 27, 3333–3336, <https://doi.org/10.1029/2000GL011581>,  
1149 2000.  
1150

1151 Pease, P. P., Tchakerian, V. P., and Tindale, N. W.: Aerosols over the Arabian Sea: geochemistry and  
1152 source areas for Aeolian desert dust, *J. Arid Environ.*, 39, 477–496,  
1153 <https://doi.org/10.1006/jare.1997.0368>, 1998.  
1154

1155 Pérez, C., Nickovic, S., Pejanovic, G., Baldasano, J. M., and Özsoy, E.: Interactive dust-radiation  
1156 modeling: A step to improve weather forecasts, *J. Geophys. Res.*, 111, 1–17, 2006.  
1157

1158 Pérez García-Pando, C., Stanton, M. C., Diggle, P. J., Trzaska, S., Miller, R. L., Perlwitz, J. P.,  
1159 Baldasano, J. M., Cuevas, E., Ceccato, P., Yaka, P., and Thomson, M. C.: Soil Dust Aerosols and  
1160 Wind as Predictors of Seasonal Meningitis Incidence in Niger, *Environ. Health Perspect.*, 122, 679–  
1161 686, doi:10.1289/ehp.1306640, 2014a.  
1162

1163 Pérez García-Pando, C., Thomson, M.C., Stanton, M., Diggle, P., Hopson, T., Pandya, R. and Miller,  
1164 R.L.: Meningitis and climate: From science to practice. *Earth Perspect.*, 1, 14, doi:10.1186/2194-  
1165 6434-1-14, 2014b.  
1166

1167 Peyridieu, S., Chédin, A., Capelle, V., Tsamalis, C., Pierangelo, C., Armante, R., Crevoisier, C.,  
1168 Crépeau, L., Siméon, M., Ducos, F., and Scott, N. A.: Characterisation of dust aerosols in the infrared  
1169 from IASI and comparison with PARASOL, MODIS, MISR, CALIOP, and AERONET observations,  
1170 *Atmos. Chem. Phys.*, 13, 6065-6082, <https://doi.org/10.5194/acp-13-6065-2013>, 2013.  
1171

1172 Piketh, S., Annegarn, H., and Tyson, P.: Lower tropospheric aerosol loadings over South Africa: the  
1173 relative contribution of aeolian dust, industrial emissions, and biomass burning, *J. Geophys. Res.*, 104,  
1174 1597–1607, 1999.  
1175

1176 Prasad, A. K., Singh, S., Chauhan, S., Srivastava, M. K., Singh, R. P., and Singh, R.: Aerosol radiative  
1177 forcing over the IndoGangetic plains during major dust storms, *Atmos. Environ.*, 41, 6289–6301,  
1178 doi:10.1016/j.atmosenv.2007.03.060, 2007a.  
1179

1180 Prasad, A. K. and Singh, R. P.: Changes in aerosol parameters during major dust storm events (2001–  
1181 2005) over the Indo-Gangetic Plains using AERONET and MODIS data, *J. Geophys. Res.- Atmos.*,  
1182 112, D09208, <https://doi.org/10.1029/2006JD007778>, 2007b.  
1183

1184 Proestakis, E., Amiridis, V., Marinou, E., Georgoulas, A. K., Solomos, S., Kazadzis, S., Chimot, J.,  
1185 Che, H., Alexandri, G., Biniotoglou, I., Daskalopoulou, V., Kourtidis, K. A., de Leeuw, G., and van  
1186 der A, R. J.: Nine-year spatial and temporal evolution of desert dust aerosols over South and East  
1187 Asia as revealed by CALIOP, *Atmos. Chem. Phys.*, 18, 1337-1362, [https://doi.org/10.5194/acp-18-](https://doi.org/10.5194/acp-18-1337-2018)  
1188 1337-2018, 2018.  
1189

1190 Prospero, J. M.: Long-range transport of mineral dust in the global atmosphere: Impact of African  
1191 dust on the environment of the southeastern United States, *P. Natl. Acad. Sci. USA*, 96, 3396–3403,  
1192 1999.  
1193

1194 Prospero, J. M., Collard, F. X., Molinie, J., and Jeannot, A.: Characterizing the annual cycle of  
1195 African dust transport to the Caribbean Basin and South America and its impact on the environment  
1196 and air quality, *Global Biogeochem. Cy.*, 28, 757–773, <https://doi.org/10.1002/2013gb004802>, 2014.  
1197

1198 Prospero, J. M., Ginoux, P., Torres, O., Nicholson, S. E., and Gill, T. E.: Environmental  
1199 characterization of global sources of atmospheric soil dust identified with the Nimbus 7 Total Ozone  
1200 Mapping Spectrometer (TOMS) absorbing aerosol product, *Rev. Geophys.*, 40, 2-1–2-31, 2002.  
1201

1202 Prospero, J. M. and Lamb, P. J.: African droughts and dust transport to the Caribbean: climate change  
1203 implications, *Science*, 302,1024–1027, doi:10.1126/science.1089915, 2003.  
1204

1205 Querol X., Tobías, A., Pérez, N., Karanasiou, A., Amato, F., Stafoggia, M., Pérez García-Pando, C.,  
1206 Ginoux, P., Forastiere, F., Gummy, S., Mudu, P., Alastuey, A.: Monitoring the impact of desert dust  
1207 outbreaks for air quality for health studies, *Environ Int.*, 130:104867, doi:  
1208 10.1016/j.envint.2019.05.061. Epub 2019 Jun 14. PMID: 31207476; PMCID: PMC6686079, 2019.  
1209

1210 Ramaswamy, V.P., Muraleedharan, M., Prakash Babu, C.: Mid-troposphere transport of Middle-East  
1211 dust over the Arabian Sea and its effect on rainwater composition and sensitive ecosystems over India.  
1212 *Scientific Reports* 7, 13676, <https://doi.org/10.1038/s41598-017-13652-1>, 2017.  
1213

1214 Rajot, J. L., Formenti, P., Alfaro, S., Desboeufs, K., Chevaillier, S., Chatenet, B., Gaudichet, A.,  
1215 Journet, E., Marticorena, B., Triquet, S., Maman, A., Mouget, N., and Zakou, A.: AMMA dust  
1216 experiment: An overview of measurements performed during the dry season special observation  
1217 period (SOP0) at the Banizoumbou (Niger) supersite, *J. Geophys. Res.*, 113, D00C14,  
1218 doi:10.1029/2008jd009906, 2008.

1219 Rashki, A., Kaskaoutis, D.G., Francois, P., Kosmopoulos, P.G., Legrand, M.: Dust-storm dynamics  
1220 over Sistan region, Iran: seasonality, transport characteristics and affected areas, *Aeol. Res.*, 16, 35–  
1221 48, 2015.

1222 Ridley, D. A., Heald, C. L., Kok, J. F., and Zhao, C.: An observationally constrained estimate of  
1223 global dust aerosol optical depth, *Atmos. Chem. Phys.*, 16, 15097–15117,  
1224 <https://doi.org/10.5194/acp-16-15097-2016>, 2016.  
1225

1226 Rivera Rivera, N. I., Gill, T. E., Gebhart, K. A., Hand, J. L., Bleiweiss, M. P., and Fitzgerald, R. M.:  
1227 Wind modeling of Chihuahuan Desert dust outbreaks, *Atmos. Environ.*, 43(2), 347–354,  
1228 doi:10.1016/j.atmosenv.2008.09.069, 2009.  
1229

1230 Rodríguez, S., Cuevas, E., Prospero, J. M., Alastuey, A., Querol, X., López-Solano, J., García, M. I.,  
1231 and Alonso-Pérez, S.: Modulation of Saharan dust export by the North African dipole, *Atmos. Chem.*  
1232 *Phys.*, 15, 7471–7486, <https://doi.org/10.5194/acp-15-7471-2015>, 2015.  
1233

1234 Rohrmann, A., Heermance, R., Kapp, P., and Cai, F. L.: Wind as the primary driver of erosion in the  
1235 Qaidam Basin, China. *Earth Planet. Sci. Lett.*, 374, 1–10, <https://doi.org/10.1016/j.epsl.2013.03.011>,  
1236 2013.  
1237

1238 Saiko, T.A., Zonn, I.S.: Irrigation expansion and dynamics of desertification in the circum-aral region  
1239 of central Asia, *Appl. Geogr.*, 20, 349–367, 2000.  
1240

1241 Sayer, A. M. and Knobelspiesse, K. D.: How should we aggregate data? Methods accounting for the  
1242 numerical distributions, with an assessment of aerosol optical depth, *Atmos. Chem. Phys.*, 19, 15023–  
1243 15048, <https://doi.org/10.5194/acp-19-15023-2019>, 2019.  
1244

1245 Schepanski, K., Tegen, I., Laurent, B., Heinold, B., and Macke, A.: A new Saharan dust source  
1246 activation frequency map derived from MSG-SEVIRI IR channels, *Geophys. Res. Lett.*, 34, L18803,  
1247 <https://doi.org/10.1029/2007GL030168>, 2007.

1248

1249 Schepanski, K., Tegen, I., Todd, M. C., Heinold, B., Bönisch, G., Laurent, B., and Macke, A.:  
1250 Meteorological processes forcing Saharan dust emission inferred from MSG-SEVIRI observations of  
1251 subdaily dust source activation and numerical models, *J. Geophys. Res.-Atmos.*, 114, D10201,  
1252 <https://doi.org/10.1029/2008JD010325>, 2009.

1253

1254 Schepanski, K., Heinold, B., and Tegen, I.: Harmattan, Saharan heat low, and West African monsoon  
1255 circulation: modulations on the Saharan dust outflow towards the North Atlantic, *Atmos. Chem.  
1256 Phys.*, 17, 10223-10243, <https://doi.org/10.5194/acp-17-10223-2017>, 2017.

1257

1258 Shen, H., Abuduwaili, J., Samat, A., Ma, L.: A review on the research of modern aeolian dust in  
1259 Central Asia, *Arab J Geosci.*, 9:625, 2016.

1260

1261 Sogacheva, L., de Leeuw, G., Rodriguez, E., Kolmonen, P., Georgoulias, A. K., Alexandri, G.,  
1262 Kourtidis, K., Proestakis, E., Marinou, E., Amiridis, V., Xue, Y., and van der A, R. J.: Spatial and  
1263 seasonal variations of aerosols over China from two decades of multi-satellite observations – Part 1:  
1264 ATSR (1995–2011) and MODIS C6.1 (2000–2017), *Atmos. Chem. Phys.*, 18, 11389-11407,  
1265 <https://doi.org/10.5194/acp-18-11389-2018>, 2018.

1266

1267 Sokolik, I. N. and Toon, O. B.: Direct radiative forcing by anthropogenic airborne mineral aerosols,  
1268 *Nature*, 381, 681–683, <https://doi.org/10.1038/381681a0>, 1996.

1269

1270 Song, Q., Zhang, Z., Yu, H., Ginoux, P., and Shen, J.: Global dust optical depth climatology derived  
1271 from CALIOP and MODIS aerosol retrievals on decadal timescales: regional and interannual  
1272 variability, *Atmos. Chem. Phys.*, 21, 13369–13395, <https://doi.org/10.5194/acp-21-13369-2021>,  
1273 2021.

1274

1275 Srivastava, A. K., Tiwari, S., Devara, P. C. S., Bisht, D. S., Srivastava, M. K., Tripathi, S. N., Goloub,  
1276 P., and Holben, B. N.: Pre-monsoon aerosol characteristics over the Indo-Gangetic Basin:  
1277 implications to climatic impact, *Ann. Geophys.*, 29, 789-804, [https://doi.org/10.5194/angeo-29-789-](https://doi.org/10.5194/angeo-29-789-2011)  
1278 2011, 2011.

1279

1280 Stanelle, T., Bey, I., Raddatz, T., Reick, C., and Tegen, I.: Anthro- pogenically induced changes in  
1281 twentieth century mineral dust burden and the associated impact on radiative forcing, *J. Geo-  
1281 Res.-Atmos.*, 119, 13526–13546, 2014.

1282 Stefanski, R. and Sivakumar, M. V. K.: Impacts of sand and dust storms on agriculture and potential  
1283 agricultural applications of a SDSWS, IOP Conf. Ser.: Earth Environ. Sci., 7, 012016, doi:  
1284 10.1088/1755-1307/7/1/012016, 2009.

1285

1286 Sun, Y., Chen, H., Tada, R., Weiss, D., Lin, M., Toyoda, S., Yan, Y., and Isozaki, Y.: ESR signal  
1287 intensity and crystallinity of quartz from Gobi and sandy deserts in East Asia and implication for  
1288 tracing Asian dust provenance, *Geochem. Geophys. Geosy.*, 14, 2615–2627,  
1289 <https://doi.org/10.1002/ggge.20162>, 2013.

1290

1291 Tanaka, T. Y. and Chiba, M.: A numerical study of the contributions of dust source regions to the  
1292 global dust budget, *Global Planet Change*, 52, 88–104,  
1293 <https://doi.org/10.1016/j.gloplacha.2006.02.002>, 2006.

1294 Tegen, I., Werner, M., Harrison, S., and Kohfeld, K.: Relative im- portance of climate and land use  
1295 in determining present and fu- ture global soil dust emission, *Geophys. Res. Lett.*, 31, L05105,  
1296 <https://doi.org/10.1029/2003GL019216>, 2004.

1297 Tegen, I., Heinold, B., Todd, M., Helmert, J., Washington, R., and Dubovik, O.: Modelling soil dust  
1298 aerosol in the Bodélé depression during the BoDEx campaign, *Atmos. Chem. Phys.*, 6, 4345–4359,  
1299 <https://doi.org/10.5194/acp-6-4345-2006>, 2006.

1300

1301 Tong, D. Q., Wang, J. X. L., Gill, T. E., Lei, H., and Wang, B. Y.: Intensified dust storm activity and  
1302 Valley fever infection in the southwestern United States, *Geophys. Res. Lett.*, 44, 4304–4312,  
1303 <https://doi.org/10.1002/2017gl073524>, 2017.

1304

1305 Tyson, P.D., Garstang, M., Swap, R., Kallberg, P., Edwards, M.: An air transport climatology for  
1306 subtropical southern Africa. *Int. J. Climatol.* 16 (3), 265–291, 1996.

1307

1308 Vickery, K. J., Eckardt, F. D., and Bryant, R. G.: A sub-basin scale dust plume source frequency  
1309 inventory for south-ern Africa, 2005–2008, *Geophys. Res. Lett.*, 40, 5274–5279,  
1310 doi:10.1002/grl.50968, 2013.

1311

1312 Voss, K. K., and Evan, A. T.: A new satellite-based global climatology of dust aerosol optical depth.  
1313 *Journal of Applied Meteorology and Climatology*, doi:10.1175/jamc-d-19-0194.1, 2020.

1314

1315 Wagener, T., Guieu, C., Losno, R., Bonnet, S., and Mahowald, N.: Revisiting atmospheric dust export  
1316 to the Southern Hemisphere ocean: Biogeochemical implications, *Glob. Biogeochem. Cy.*, 22,  
1317 GB2006, <https://doi.org/10.1029/2007gb002984>, 2008.

1318

1319 Washington, R., Todd, M., Middleton, N. J., and Goudie, A. S.: Dust-storm source areas determined  
1320 by the total ozone monitoring spectrometer and surface observations, *Ann. Assoc. Am. Geogr.*, 93,  
1321 297–313, <https://doi.org/10.1111/1467-8306.9302003>, 2003.

1322

1323 Washington, R. and Todd, M. C.: Atmospheric controls on mineral dust emission from the Bodélé  
1324 depression, Chad: The role of the low level jet, *Geophys. Res. Lett.*, 32, L17701,  
1325 <https://doi.org/10.1029/2005GL023597>, 2005.

1326

1327 Washington, R., Bouet, C., Cautenet, G., Mackenzie, E., Ashpole, I., Engelstaedter, S., Lizcano, G.,  
1328 Henderson, G. M., Schepanski, K., and Tegen, I.: Dust as a tipping element: the Bodélé Depression,  
1329 Chad, *P. Natl. Acad. Sci. USA*, 106, 20564–20571, doi:10.1073/pnas.0711850106, 2009.

1330

1331 Weinzierl, B., Sauer, D., Minikin, A., Reitebuch, O., Dahlkotter, F., Mayer, B., Emde, C., Tegen, I.,  
1332 Gasteiger, J., Petzold, A., Veira, A., Kueppers, U., and Schumann, U.: On the visibility of airborne  
1333 volcanic ash and mineral dust from the pilot's perspective in flight, *Phys Chem Earth*, 45-46, 87-102,  
1334 10.1016/j.pce.2012.04.003, 2012.

1335

1336 Winker, D. M., Vaughan, M. A., Omar, A., Hu, Y., Powell, K. A., Liu, Z., Hunt, W. H. and Young,  
1337 S. A.: Overview of the CALIPSO Mission and CALIOP Data Processing Algorithms, *J. Atmos.*  
1338 *Oceanic Technol.*, 26(11), 2310–2323, doi:10.1175/2009JTECHA1281.1, 2009.

1339

1340 Yu, H. B., Chin, M., Winker, D. M., Omar, A. H., Liu, Z. Y., Kittaka, C., and Diehl, T.: Global view  
1341 of aerosol vertical distributions from CALIPSO lidar measurements and GOCART simulations:  
1342 Regional and seasonal variations, *J. Geophys. Res.-Atmos.*, 115, D00H30,  
1343 <https://doi.org/10.1029/2009jd013364>, 2010.

1344

1345 Yu, H. B., Chin, M., Yuan, T. L., Bian, H. S., Remer, L. A., Prospero, J. M., Omar, A., Winker, D.,  
1346 Yang, Y. K., Zhang, Y., Zhang, Z. B., and Zhao, C.: The fertilizing role of African dust in the Amazon  
1347 rainforest: A first multiyear assessment based on data from Cloud-Aerosol Lidar and Infrared  
1348 Pathfinder Satellite Observations, *Geophys. Res. Lett.*, 42, 1984–1991,  
1349 <https://doi.org/10.1002/2015gl063040>, 2015.

1350

1351 Yu, H., Remer, L. A., Chin, M., Bian, H., Kleidman, R. G., and Diehl, T.: A satellite-based assessment  
1352 of transpacific transport of pollution aerosol, *J. Geophys. Res.-Atmos.*, 113, D14S12,  
1353 <https://doi.org/10.1029/2007JD009349>, 2008.

1354

1355 Yu, Y., Kalashnikova, O. V., Garay, M. J., and Notaro, M.: Climatology of Asian dust activation and  
1356 transport potential based on MISR satellite observations and trajectory analysis, *Atmos. Chem. Phys.*,  
1357 19, 363-378, <https://doi.org/10.5194/acp-19-363-2019>, 2019.

1358

1359 Yu, Y., Notaro, M., Kalashnikowa, O., Garay, M.: Climatology of summer Shamal wind in the  
1360 Middle East, *J. Geophys. Res.-Atmos.* 121 (1), 289–305, 2016.

1361

1362 Yu, Y., Notaro, M., Liu, Z., Kalashnikova, O., Alkolibi, F., Fadda, E., and Bakhrjy, F.: Assessing  
1363 temporal and spatial variations in atmospheric dust over Saudi Arabia through satellite, radiometric,  
1364 and station data, *J. Geophys. Res.-Atmos.*, 118, 13253– 13264,  
1365 <https://doi.org/10.1002/2013JD020677>, 2013.

1366

1367 Yu, Y., Kalashnikova, O. V., Garay, M. J., Lee, H., Choi, M., Okin, G. S., Yorks, J. E., Campbell, J.  
1368 R., and Marquis, J.: A global analysis of diurnal variability in dust and dust mixture using CATS  
1369 observations, *Atmos. Chem. Phys.*, 21, 1427–1447, <https://doi.org/10.5194/acp-21-1427-2021>, 2021.

1370

1371 Xi, X. and Sokolik, I. N.: Seasonal dynamics of threshold friction velocity and dust emission in  
1372 Central Asia, *J. Geophys. Res. Atmos.*, 120(4), 1536–1564, doi:10.1002/2014JD022471, 2015.

1373

1374 Zender, C. S., Huisheng, B., and Newman, D.: Mineral Dust Entrainment and Deposition (DEAD)  
1375 model: Description and 1990s dust climatology, *J. Geophys. Res.*, 108, 4416,  
1376 <https://doi.org/10.1029/2002JD002775>, 2003.

1377

1378

1379

1380

1381

1382

1383

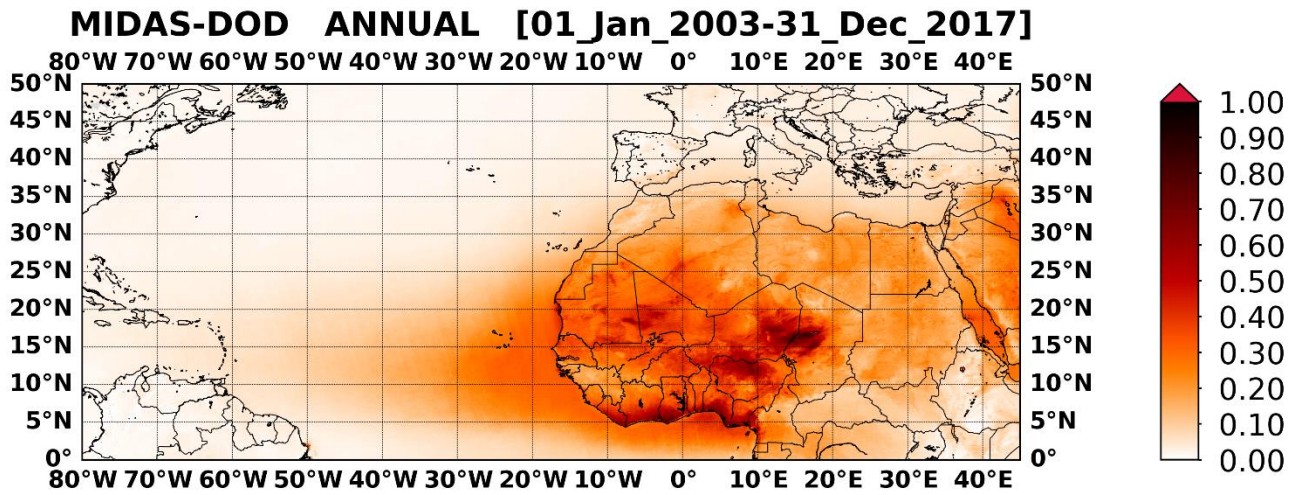
1384



1385 **Table 1:** Annual and seasonal DOD averages, representative for the period 2003-2017, along with the associated  
1386 uncertainty. The first three rows refer to the whole globe (GLB), the global land (GLB-land) and global ocean (GLB-  
1387 ocean). In the fourth and fifth line are given the results for N. Hemisphere (NHE) and S. Hemisphere (SHE) DODs  
1388 whereas in the rest 17 entries the corresponding results for selected subregions (denoted with colored rectangles in Fig. 7  
1389 in Gkikas et al. (2021)) are given.

<b>REGION</b>	<b>ANNUAL</b>	<b>DJF</b>	<b>MAM</b>	<b>JJA</b>	<b>SON</b>
<b>GLB</b>	0.032 ± 0.003	0.025 ± 0.004	0.043 ± 0.005	0.040 ± 0.005	0.022 ± 0.004
<b>GLB-land</b>	0.070 ± 0.005	0.063 ± 0.008	0.104 ± 0.011	0.083 ± 0.010	0.049 ± 0.007
<b>GLA-ocean</b>	0.019 ± 0.002	0.015 ± 0.003	0.026 ± 0.003	0.023 ± 0.003	0.012 ± 0.003
<b>NHE</b>	0.056 ± 0.004	0.043 ± 0.005	0.085 ± 0.009	0.071 ± 0.008	0.036 ± 0.005
<b>SHE</b>	0.008 ± 0.001	0.010 ± 0.003	0.008 ± 0.002	0.006 ± 0.002	0.008 ± 0.003
<b>BOD</b>	0.533 ± 0.009	0.483 ± 0.018	0.614 ± 0.020	0.603 ± 0.017	0.451 ± 0.013
<b>GOB</b>	0.092 ± 0.007	0.074 ± 0.010	0.189 ± 0.023	0.078 ± 0.010	0.056 ± 0.005
<b>CAS</b>	0.126 ± 0.007	0.084 ± 0.012	0.158 ± 0.016	0.144 ± 0.011	0.100 ± 0.007
<b>NME</b>	0.227 ± 0.006	0.120 ± 0.009	0.319 ± 0.016	0.271 ± 0.011	0.186 ± 0.009
<b>SUS</b>	0.018 ± 0.001	0.009 ± 0.002	0.033 ± 0.005	0.021 ± 0.003	0.010 ± 0.001
<b>TAK</b>	0.246 ± 0.020	0.114 ± 0.015	0.504 ± 0.047	0.259 ± 0.030	0.130 ± 0.018
<b>THA</b>	0.198 ± 0.007	0.086 ± 0.006	0.291 ± 0.013	0.424 ± 0.033	0.109 ± 0.006
<b>WSA</b>	0.302 ± 0.006	0.199 ± 0.008	0.362 ± 0.015	0.418 ± 0.016	0.237 ± 0.009
<b>EAS</b>	0.077 ± 0.005	0.072 ± 0.014	0.130 ± 0.012	0.056 ± 0.010	0.048 ± 0.006
<b>ENP</b>	0.020 ± 0.002	0.011 ± 0.002	0.047 ± 0.005	0.017 ± 0.004	0.013 ± 0.002
<b>ETA</b>	0.146 ± 0.007	0.109 ± 0.011	0.169 ± 0.015	0.202 ± 0.015	0.093 ± 0.009
<b>GOG</b>	0.309 ± 0.021	0.417 ± 0.032	0.416 ± 0.066	0.064 ± 0.021	0.100 ± 0.022
<b>MED</b>	0.081 ± 0.003	0.052 ± 0.008	0.106 ± 0.009	0.096 ± 0.006	0.066 ± 0.005
<b>SME</b>	0.250 ± 0.008	0.154 ± 0.009	0.318 ± 0.016	0.394 ± 0.020	0.166 ± 0.008
<b>SSA</b>	0.326 ± 0.013	0.309 ± 0.015	0.494 ± 0.041	0.241 ± 0.054	0.199 ± 0.020
<b>WNP</b>	0.028 ± 0.002	0.017 ± 0.003	0.064 ± 0.008	0.023 ± 0.006	0.018 ± 0.002
<b>WTA</b>	0.035 ± 0.003	0.006 ± 0.002	0.035 ± 0.005	0.090 ± 0.009	0.017 ± 0.004

1390  
1391  
1392  
1393  
1394  
1395  
1396



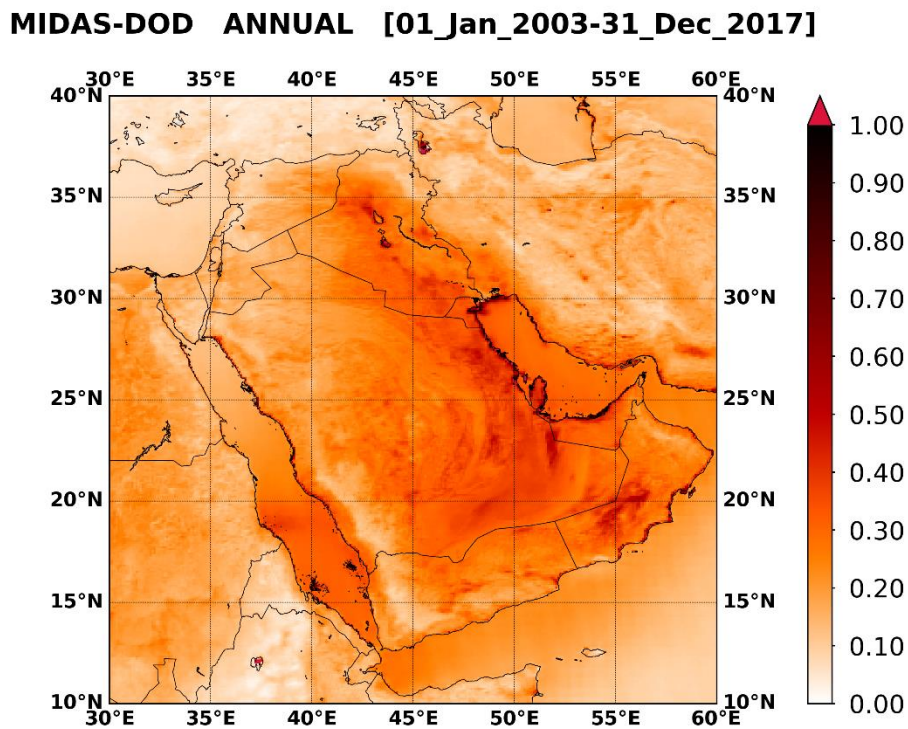
1397

1398

1399

1400

**Figure 1:** Geographical distribution of the MIDAS annual DOD at 550nm, representative for the period 1 January 2003 – 31 December 2017, over North Africa, the Tropical Atlantic Ocean and the broader Mediterranean basin.



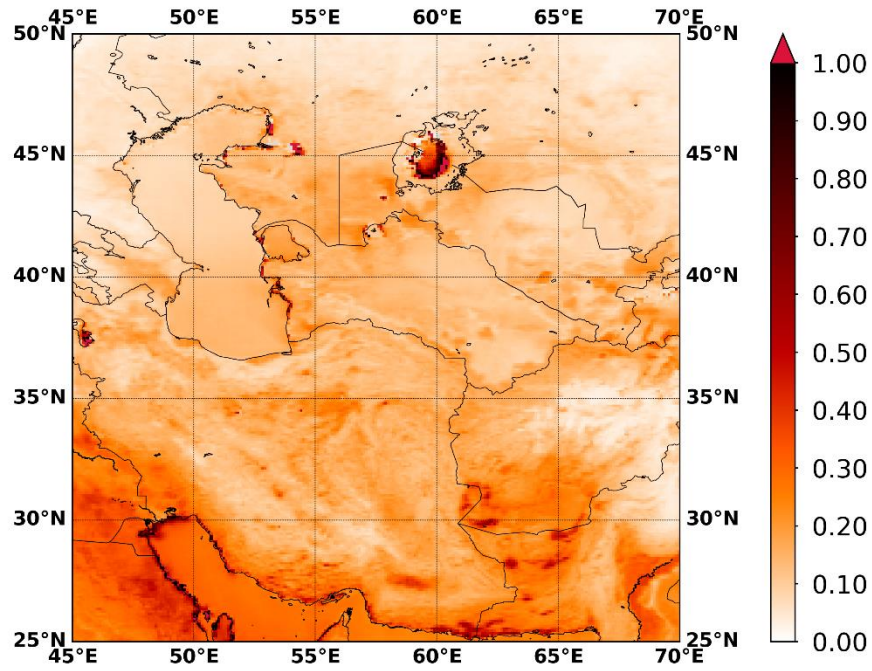
1401

1402

1403

**Figure 2:** As in Figure 1 but for the broader area of the Middle East.

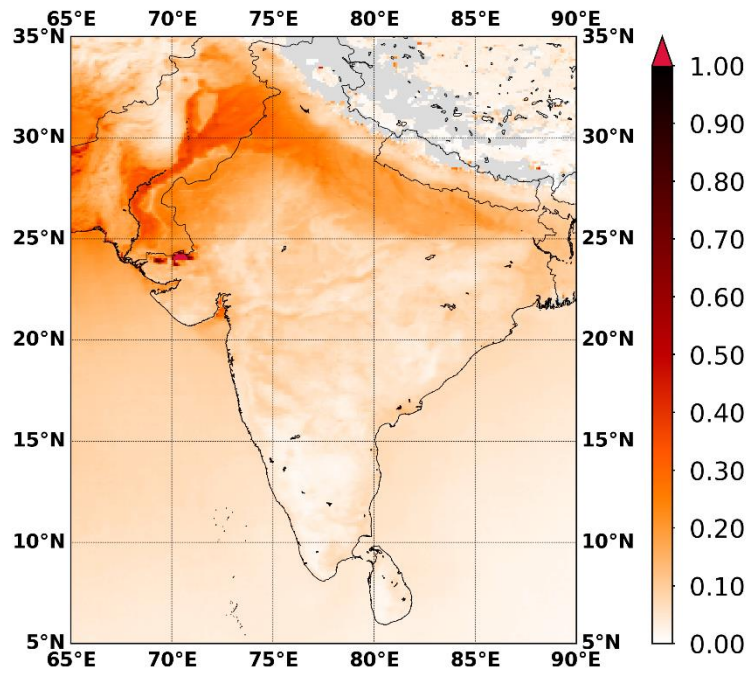
**MIDAS-DOD ANNUAL [01\_Jan\_2003-31\_Dec\_2017]**



1404  
1405  
1406

**Figure 3:** As in Figure 1 but for central and southwestern Asia.

**MIDAS-DOD ANNUAL [01\_Jan\_2003-31\_Dec\_2017]**



1407  
1408  
1409

**Figure 4:** As in Figure 1 but for the Indian subcontinent.

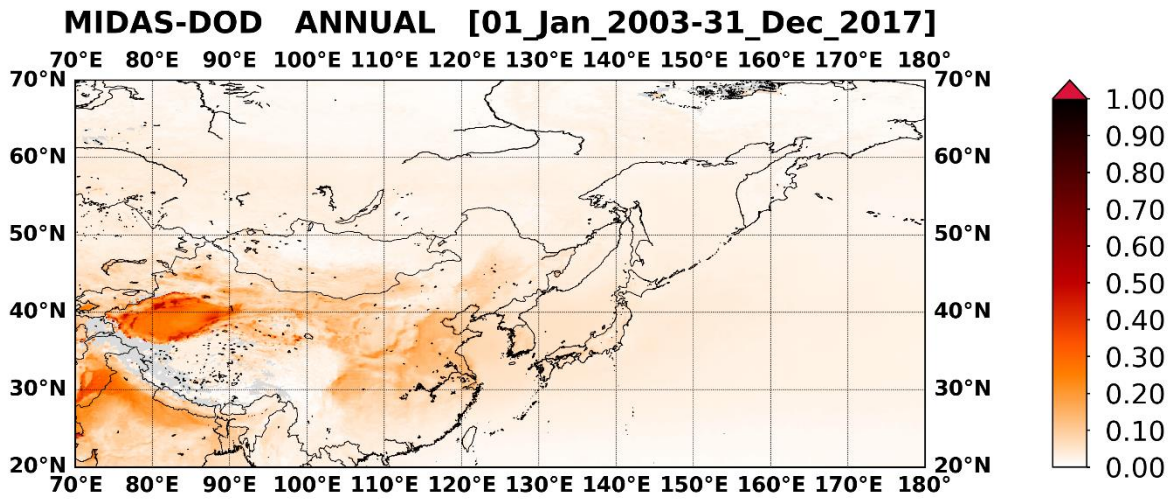


Figure 5: As in Figure 1 but for East Asia and the North Pacific Ocean.

1410  
1411  
1412

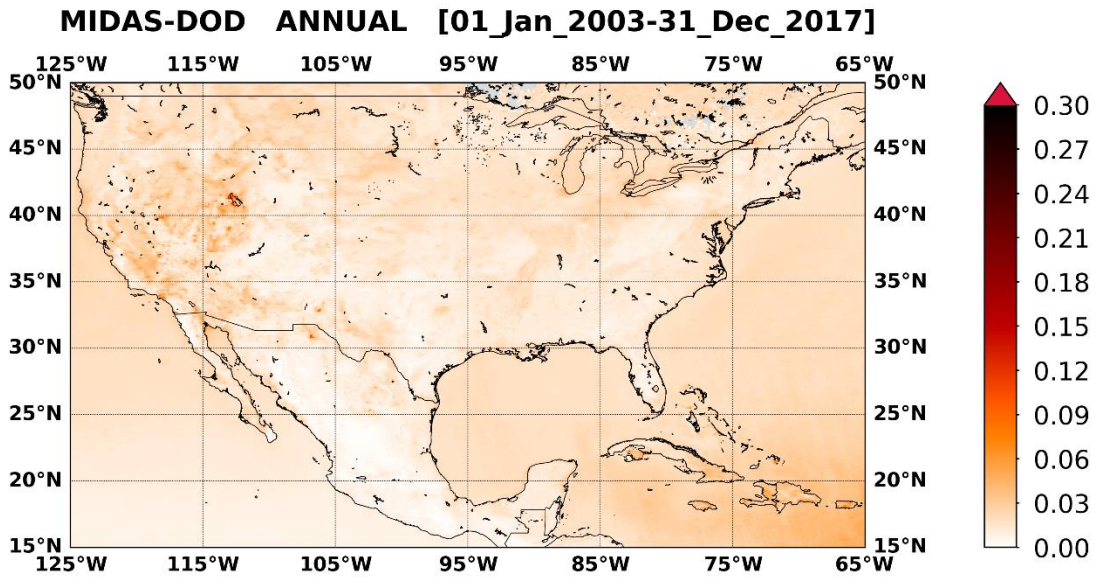


Figure 6: As in Figure 1 but for North America.

1413  
1414  
1415

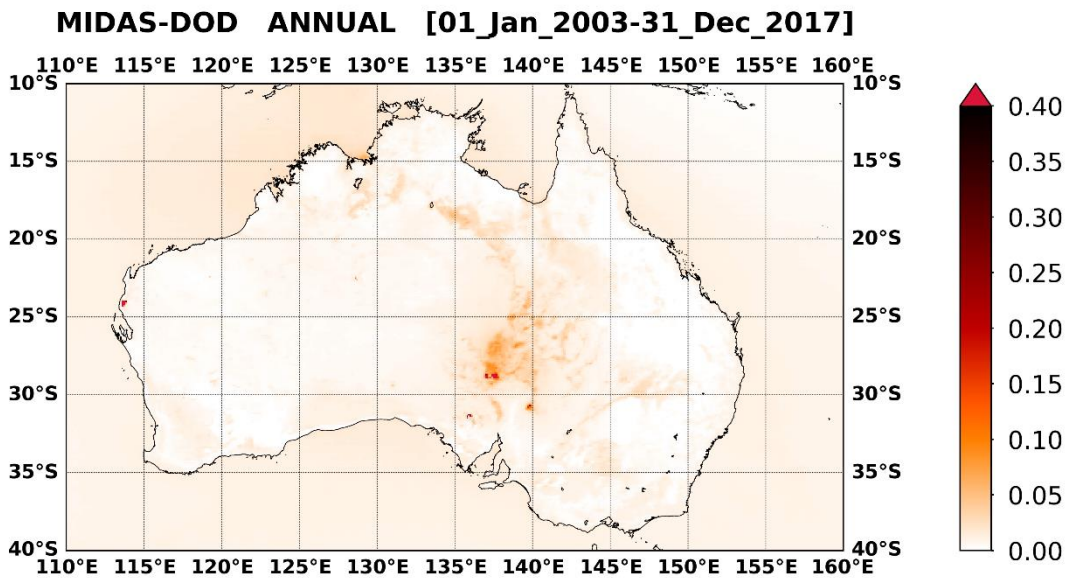
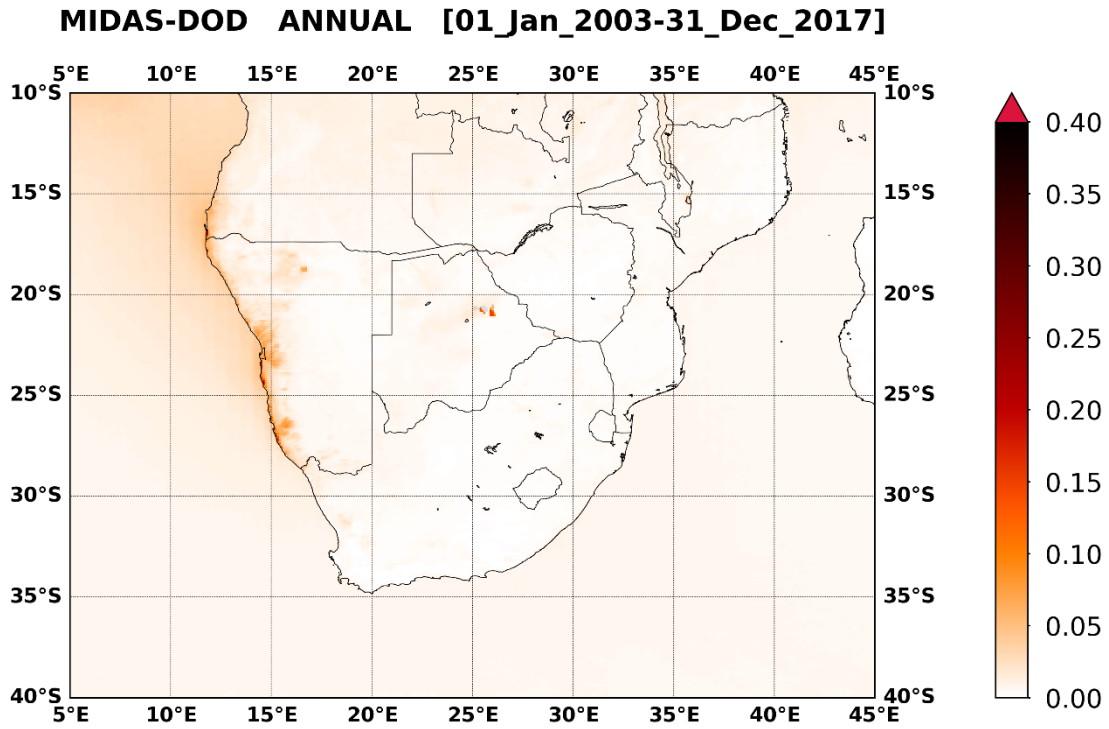


Figure 7: As in Figure 1 but for Australia.

1416  
1417  
1418

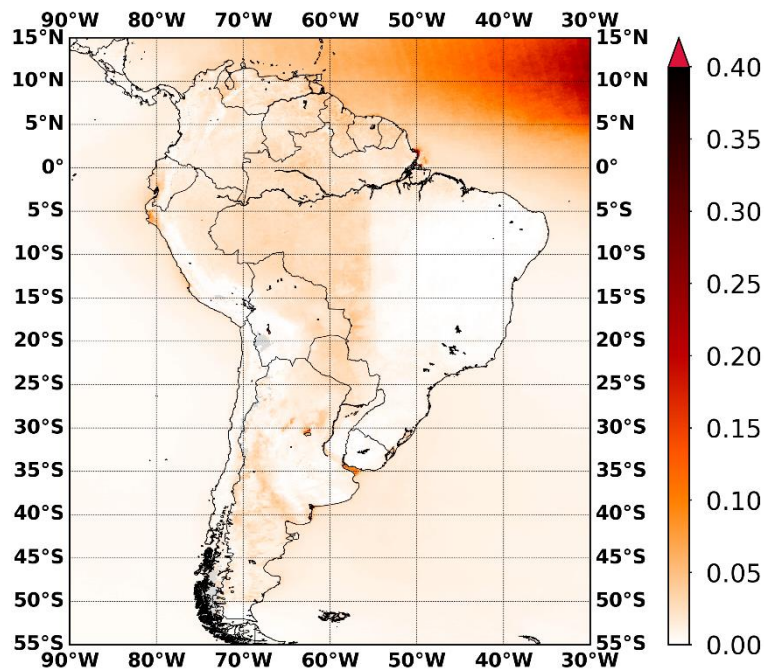
1419



1420  
1421  
1422

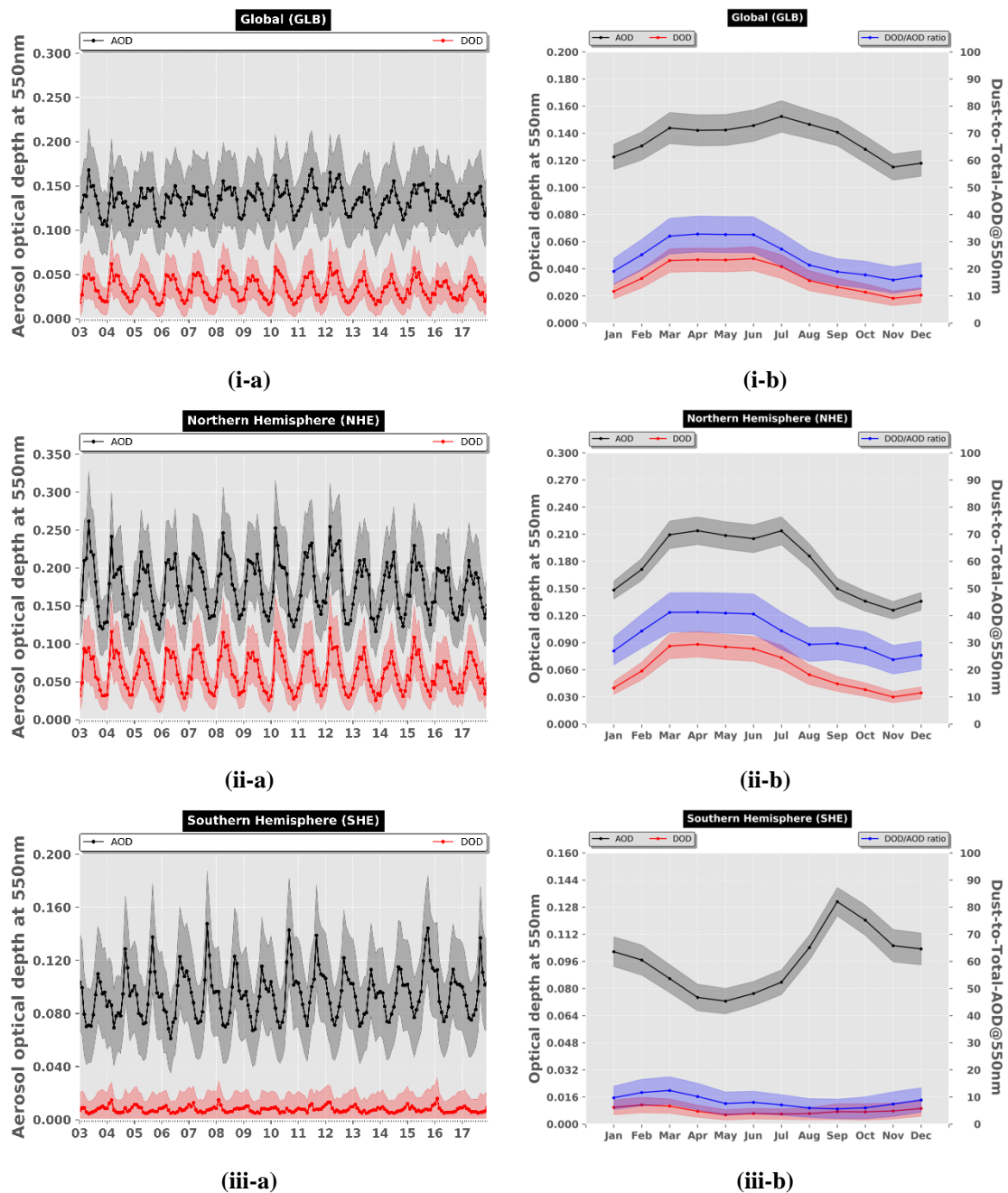
**Figure 8:** As in Figure 1 but for Southern Africa.

**MIDAS-DOD ANNUAL [01\_Jan\_2003-31\_Dec\_2017]**



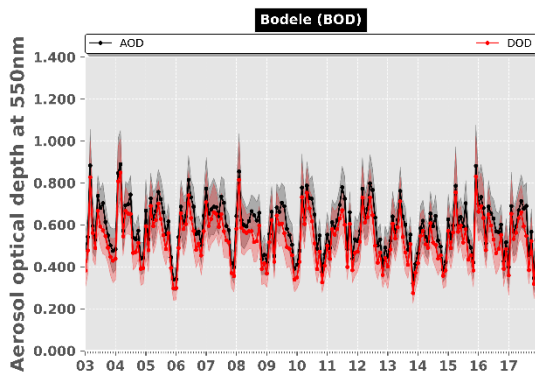
1423  
1424  
1425  
1426  
1427  
1428  
1429  
1430  
1431  
1432  
1433

**Figure 9:** As in Figure 1 but for South America.

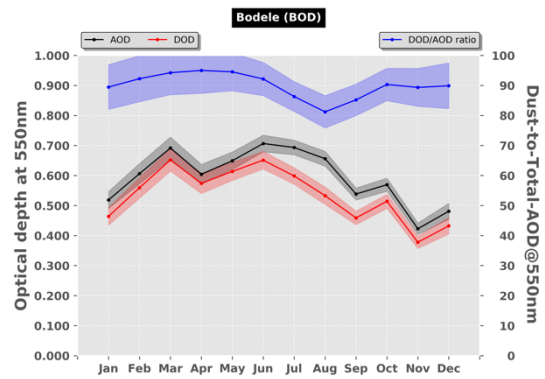


1434 **Figure 10:** Inter-annual (-a) and intra-annual (-b) variability, representative for the period 2007 – 2016, of monthly  
 1435 MODIS AOD<sub>550nm</sub> (black curve) and DOD<sub>550nm</sub> (red curve) regionally averaged for: (i) the whole globe (GLB), (ii)  
 1436 Northern Hemisphere (NHE) and (iii) the Southern Hemisphere (SHE). The blue curves in the intra-annual plots depict  
 1437 the dust-to-total AOD<sub>550nm</sub> ratio (expressed in percentage; right y-axis). The shaded areas correspond to the total  
 1438 uncertainty.

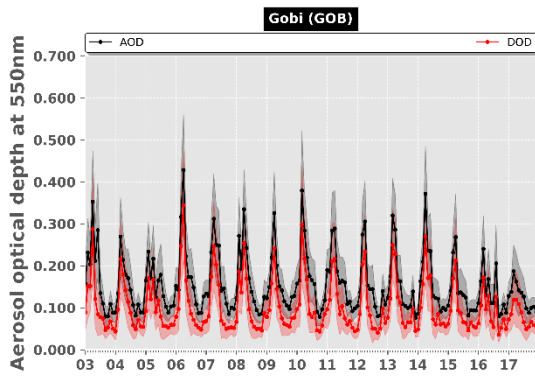
1439  
 1440  
 1441  
 1442  
 1443  
 1444  
 1445  
 1446



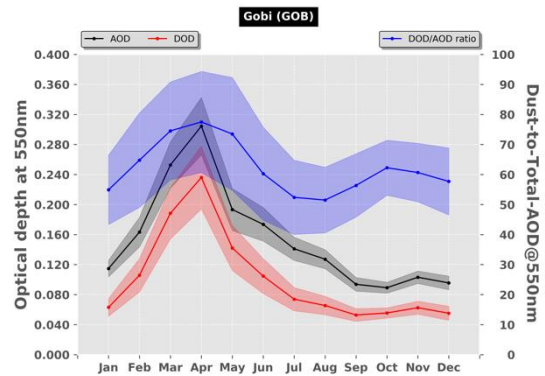
(i-a)



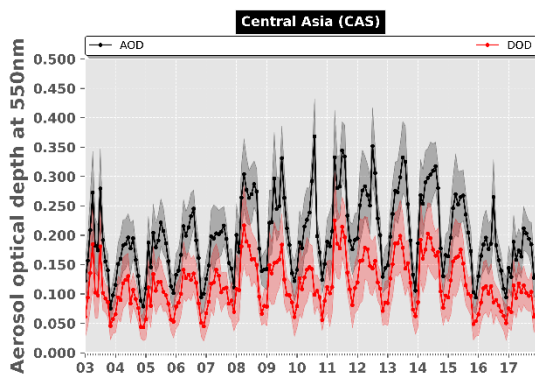
(i-b)



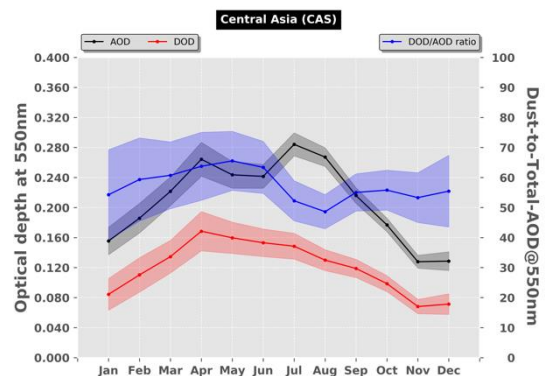
(ii-a)



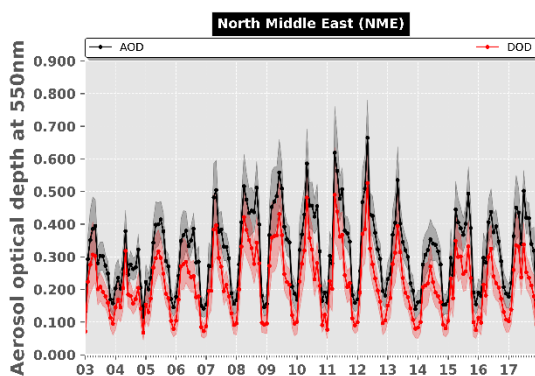
(ii-b)



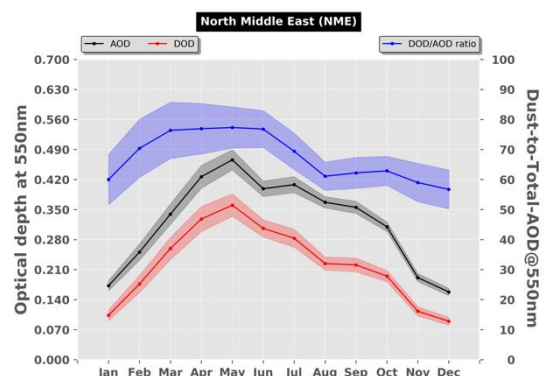
(iii-a)



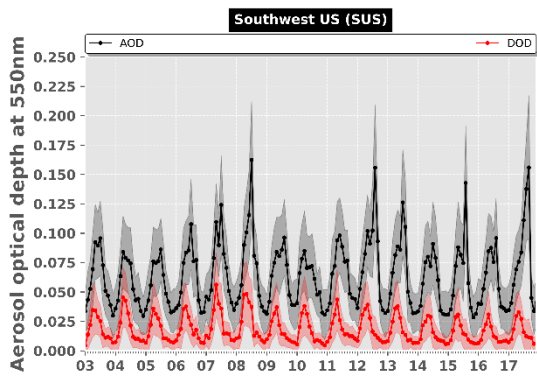
(iii-b)



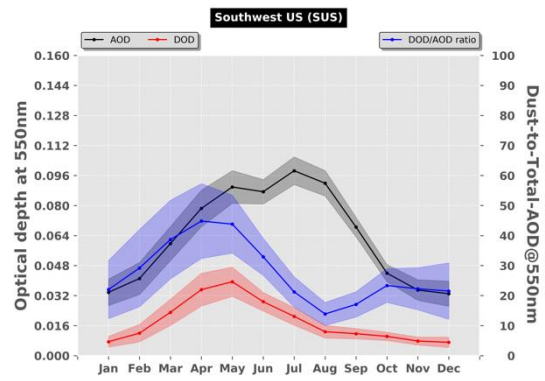
(iv-a)



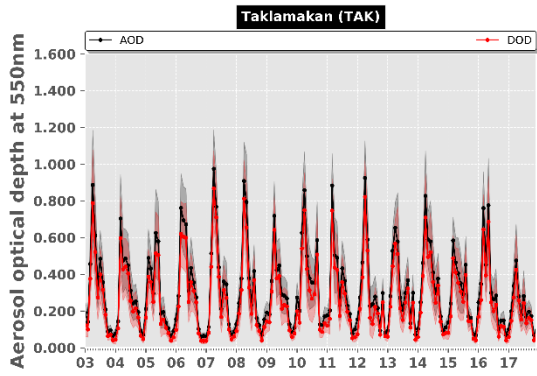
(iv-b)



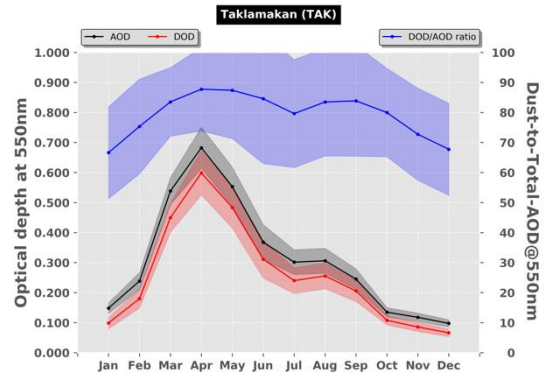
(v-a)



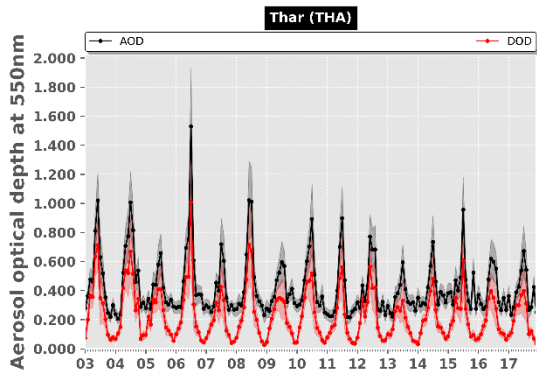
(v-b)



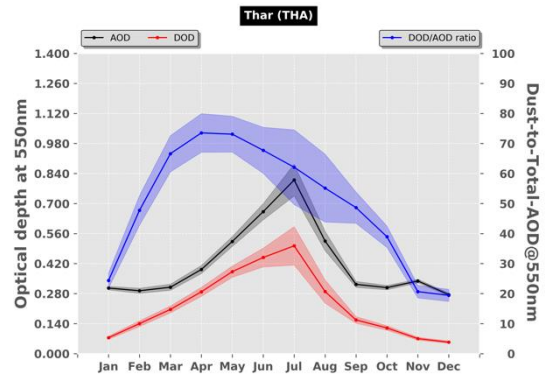
(vi-a)



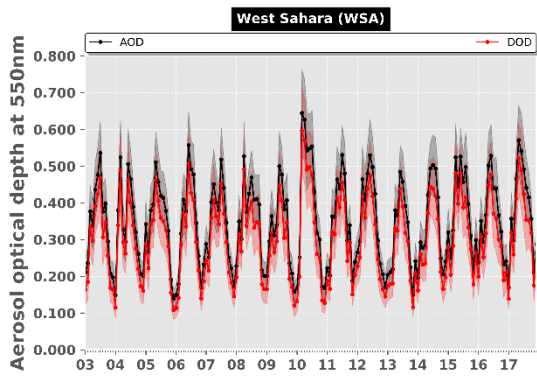
(vi-b)



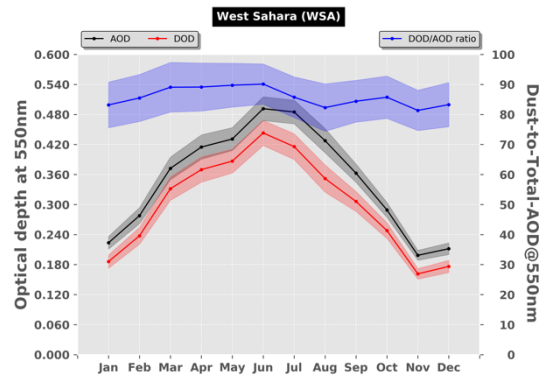
(vii-a)



(vii-b)

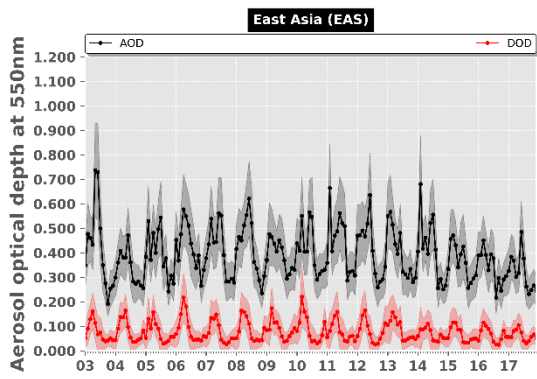


(viii-a)

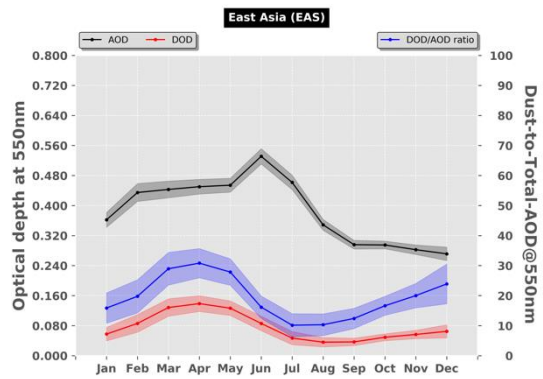


(viii-b)

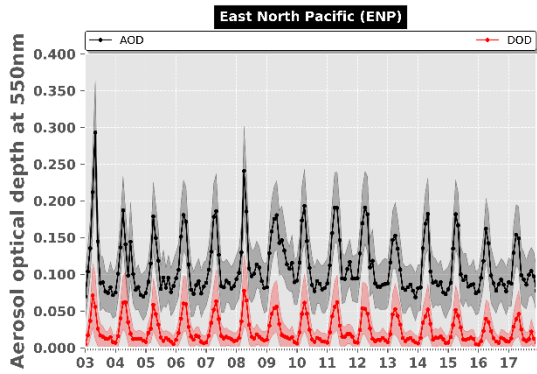




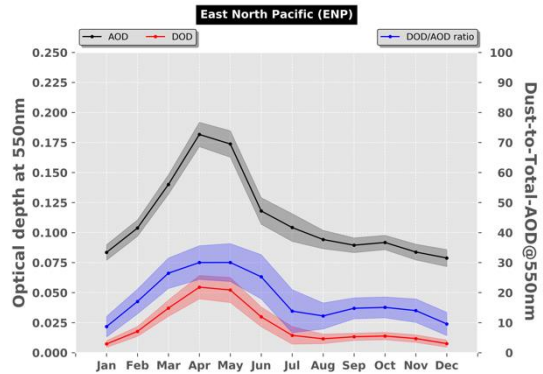
(ix-a)



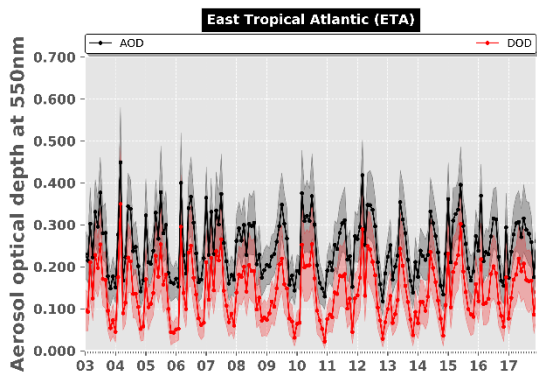
(ix-b)



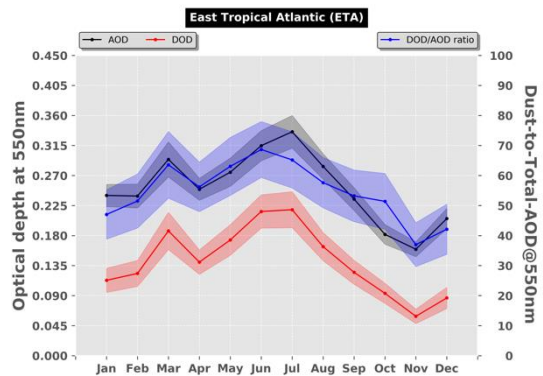
(x-a)



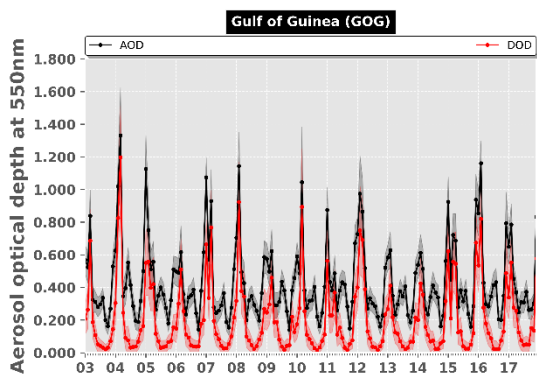
(x-b)



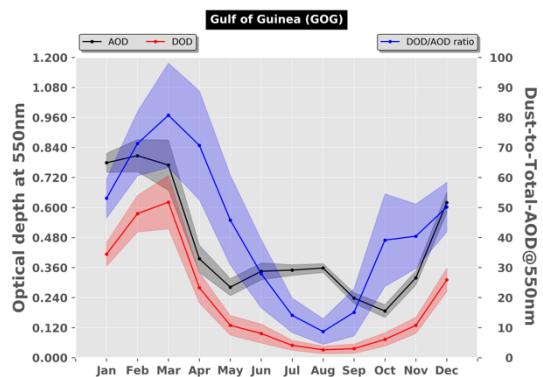
(xi-a)



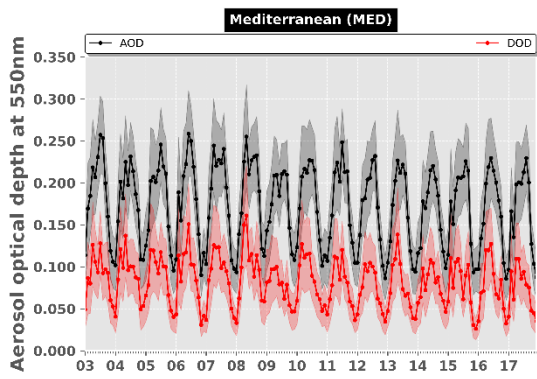
(xi-b)



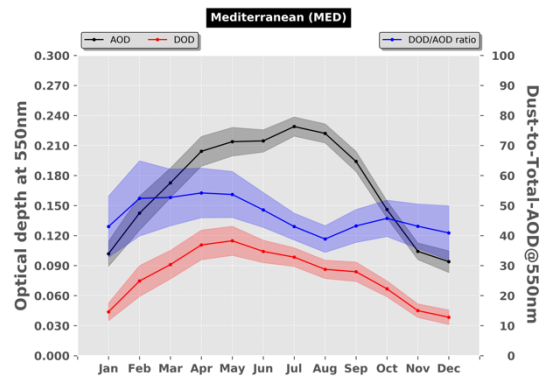
(xii-a)



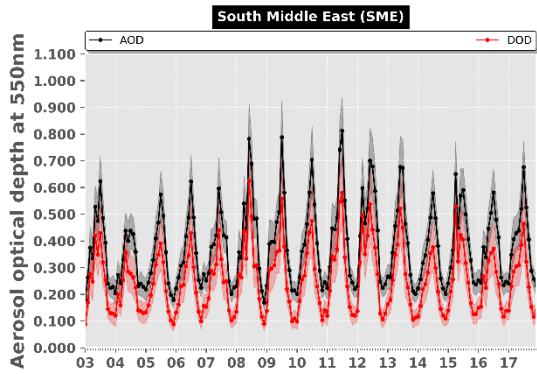
(xii-b)



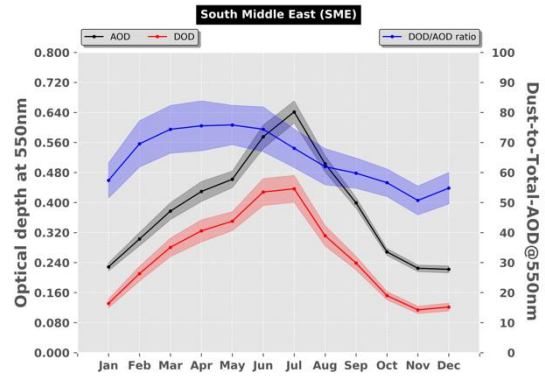
(xiii-a)



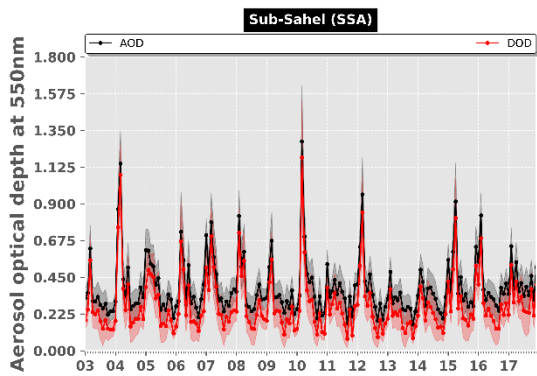
(xiii-b)



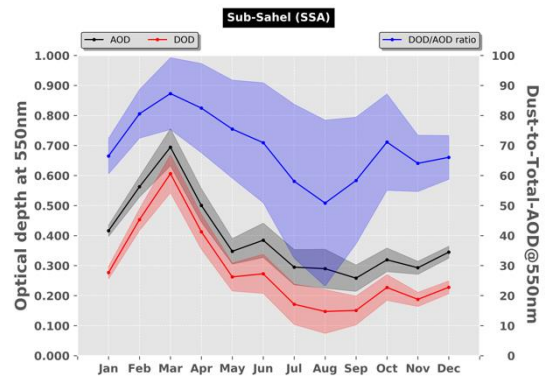
(xiv-a)



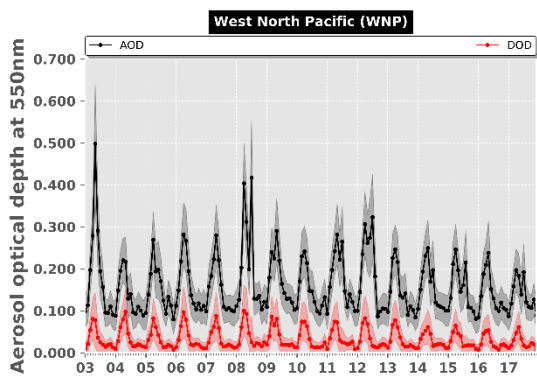
(xiv-b)



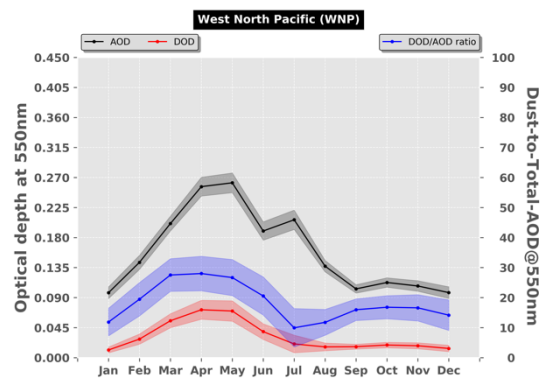
(xv-a)



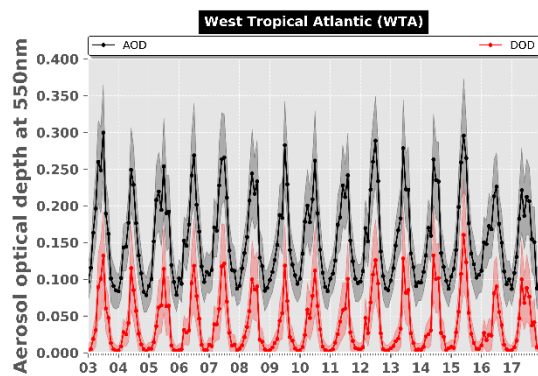
(xv-b)



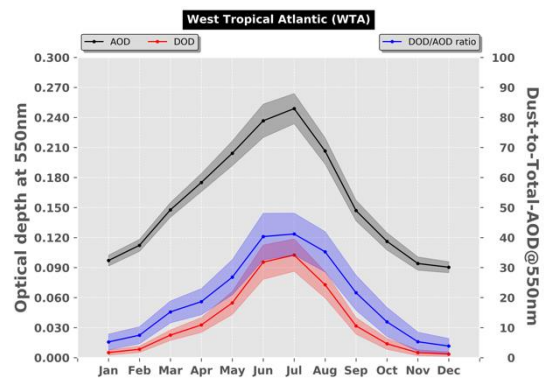
(xvi-a)



(xvi-b)



(xvii-a)



(xvii-b)

1447 **Figure 11:** Inter-annual (-a) and intra-annual (-b) variability, representative for the period 2003 – 2017, of monthly  
 1448 MODIS AOD<sub>550nm</sub> (black curve) and DOD<sub>550nm</sub> (red curve) regionally averaged for: (i) Bodélé Depression (BOD), (ii)  
 1449 Gobi Desert (GOB), (iii) Central Asia (CAS), (iv) North Middle East (NME), (v) southwest United States (SUS), (vi)  
 1450 Taklamakan Desert (TAK), (vii) Thar Desert (THA), (viii) West Sahara (WSA), (ix) East Asia (EAS), (x) East North  
 1451 Pacific (ENP), (xi) East Tropical Atlantic (ETA), (xii) Gulf of Guinea (GOG), (xiii) Mediterranean (MED), (xiv) South  
 1452 Middle East (SME), (xv) Sub-Sahel (SSA), (xvi) West North Pacific (WNP) and (xvii) West Tropical Atlantic (WTA).  
 1453 The shaded areas in the inter and intra-annual plots correspond to the total uncertainty. The blue curves in the intra-annual  
 1454 plots represent the percentage contribution of dust optical depth (DOD) to the aerosol optical depth (AOD).  
 1455  
 1456  
 1457  
 1458  
 1459  
 1460  
 1461  
 1462  
 1463  
 1464  
 1465  
 1466  
 1467  
 1468  
 1469  
 1470  
 1471  
 1472  
 1473  
 1474  
 1475  
 1476  
 1477  
 1478

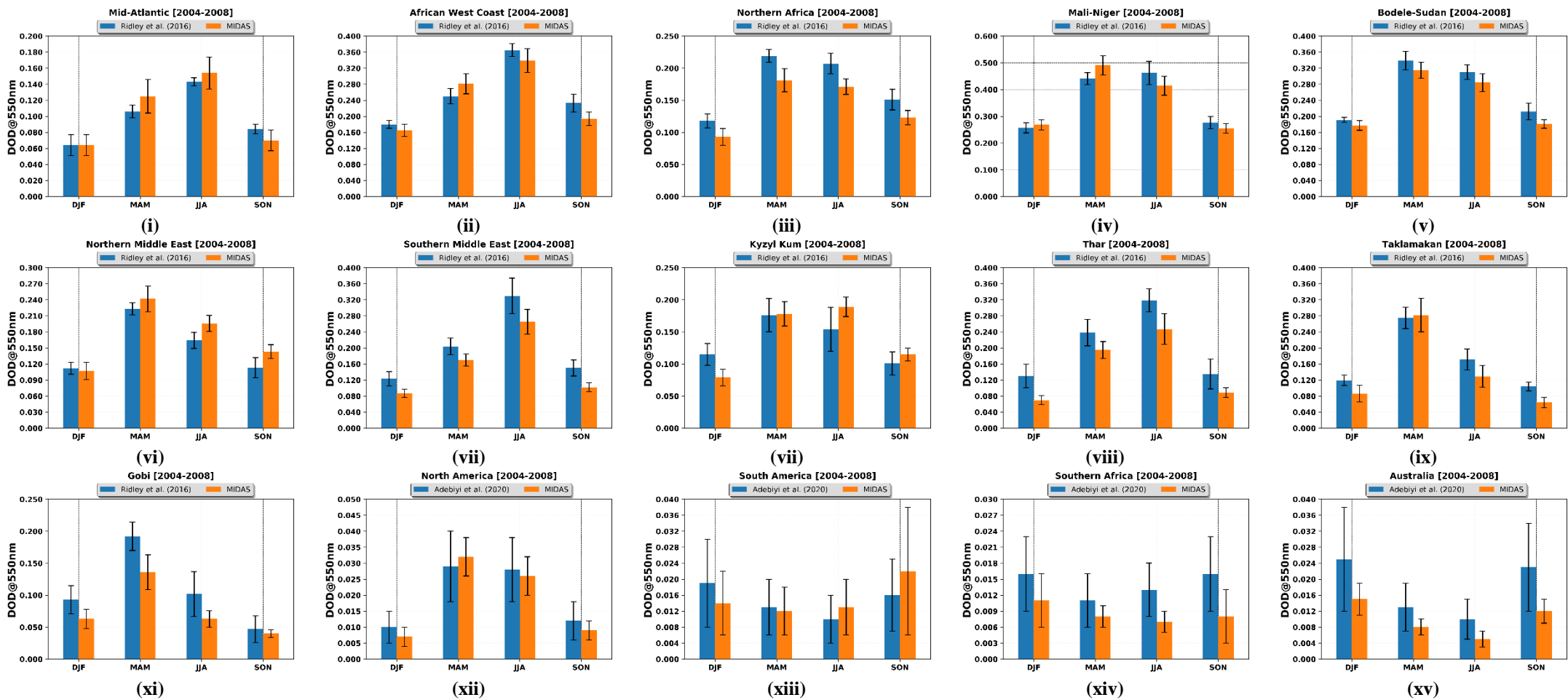


**Figure 12:** Seasonal DODs, representative for the period 2004 – 2008, based on the MIDAS dataset (orange bars), Ridley et al. (2016) (blue bars) and Adebiyi et al. (2020) (blue bars), for 15 regions (their names are given at the top of each plot) defined in Kok et al. (2021a) (see Table 2). The error bars represent the estimated uncertainties. From i to xi, the blue bars correspond to the Ridley et al. (2016) results whereas for the remaining regions MIDAS DODs are compared against the corresponding levels obtained by Adebiyi et al. (2020).